Combined Theoretical and Exprimental Chracterization of Semicondcutors for Photoelectrocatalytic Applications

Tangui Le Bahers, Kazuhiro Takanabe

Combined theoretical and experimental characterizations of semiconductors for photoelectrocatalytic applications

Tangui Le Bahers[1*] and Kazuhiro Takanabe[2*]

[1] *Univ Lyon, ENS de Lyon, CNRS, Université Claude Bernard Lyon 1, Laboratoire de Chimie UMR 5182, F-69342 Lyon, France*

[2] *Department of Chemical System Engineering, School of Engineering, The University of Tokyo, 7-3-1 Hongo, Bunkyo-ku, Tokyo, 113-8656, Japan*

Keywords: photocatalysis, absorption coefficient, exciton binding energy, effective mass, DFT

[*]Corresponding authors: T. Le Bahers (tangui.le_bahers@ens-lyon.fr) K. Takanabe (takanabe@chemsys.t.u-tokyo.ac.jp)

Abstract

Photoelectrocatalysis studies have emerged tremendous knowledge and experience, which has led to discovery of a number of active materials. Due to complexity of the processes involved, however, development of suitable semiconductor and catalyst for the photoelectrocatalysis still requires a try-and-error approach as different parameters are coherently varied to determine overall performance. This contribution provides insight into the key optoelectronic properties of the semiconductors, such as absorption coefficient, dielectric constant, effective masses, exciton binding energy, and band positions. The combined assessment from theoretical and experimental points of view is reviewed, which may help thorough understanding of the semiconductors and the way to reliably characterize them, and in turn to develop improved photoelectrocatalytic materials.

Introduction

The scientific community has devoted much effort to developing efficient photovoltaic devices that can convert sunlight (i.e., photons) into electricity (i.e., electrons and holes in an external circuit). This important topic of research has led scientists to the development of a large variety of photovoltaic materials[1–7] whose photoconversion efficiencies are compared on the frequently updated NREL chart.[8] In parallel to this research activity, the researchers developed the idea that photogenerated electrons and holes can be effectively and directly consumed to perform electrochemical redox reactions.[9,10] Such photoelectrocatalytic reactions can produce valuable molecules with the ability to generate energy on demand or valuable molecules for the chemical industry.[11–19] The two main investigated reactions are CO_2 reduction[20–22] and water splitting.[23–27] Recently, new types of photoelectrocatalytic reactions are being investigated, such as biomass valorization, among which glycerol oxidation seems most promising.[28–31]

Since water splitting is one of the most investigated reactions in photoelectrocatalysis, this manuscript is oriented toward this reaction as an excellent benchmark of the energetically uphill reaction.[32] The main concepts presented herein can be transferred to other photoelectrocatalytic reactions. Water splitting is the combination of two half-electrochemical reactions called oxygen evolution reaction (OER, equation 1) and hydrogen evolution reaction (HER, equation 2). To achieve solar-driven water splitting, multiple device configurations have been proposed.[33,34] The first solar-derived water splitting technology is simply accomplished by connecting a solar panel to an electrolyzer via an external circuit to split water and produce H_2. Another technology consists of solar panels directly immersed in water to perform OER and HER with appropriate surface modifications to make photoelectrodes,[35,36] which might not require wiring.[37] Also, photon absorbers can be

dispersed in water as a powder form with the high surface area, so-called photocatalyst, which has a dual function to absorb the sunlight and to perform the two half-reactions.[38–43]

$$2H_2O \rightarrow O_2 + 4H^+ + 4e^- \text{ or } 4OH^- \rightarrow O_2 + 2H_2O + 4e^- \quad (1)$$

$$2H^+ + 2e^- \rightarrow H_2 \text{ or } 2H_2O + 2e^- \rightarrow H_2 + 2OH^- \quad (2)$$

Multiple articles have addressed the economic viability of these water splitting technologies.[44–47] Several architectures were proposed to estimate their capital cost, assuming several working conditions. As of now, the highest efficiency for producing H_2 from sunlight is to connect two separate devices of a photovoltaic cell and an electrolyzer.[48] It is difficult to rigorously compare these studies because the assumptions made about the properties and architectures of the materials are typically different. However, it seems likely that a direct water splitting technology, using photoelectrochemical and photocatalytic systems, would be more profitable than a solar panel connected to an electrolyzer.[44] Unfortunately, despite the potential economic advantage, efficient photoelectrocatalytic materials have not yet met the requirements for commercialization.

Therefore, for this technology to be considered viable for H_2 production, it is necessary to develop efficient water splitting photoelectrocatalytic materials that are applicable to an integrated photoelectrochemical system or a photocatalyst powder system. Understanding the fundamental phenomena involved in the photocatalytic process should help to improve this efficiency. As we will see in the next section, however, this is a difficult task because of the complex elementary steps involved in the photocatalytic process.[49] This review focuses on characterization of photocatalyst powder materials, but we note that fundamental aspects for optoelectronic properties are very much in common for photoelectrochemical reactions.

Focus on the photocatalysts

Heterogeneous photocatalysts developed for overall water splitting using a single semiconductor typically have the architecture presented in Figure 1.[24,50] The photocatalyst consists of semiconductor particles decorated by cocatalyst nanoparticles to facilitate OER or HER.[51] The fundamental principles of photoelectrochemical OER or HER are generally the same under open circuit conditions. Figure 1 focuses on the respective half-reactions.

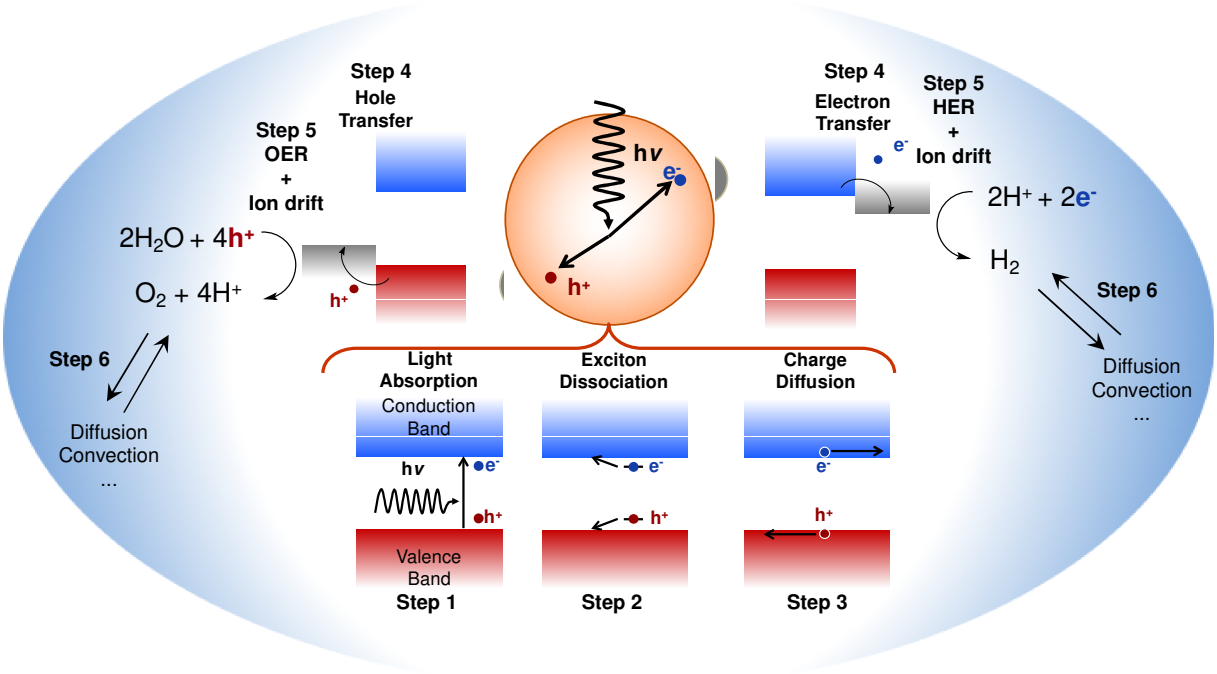

Figure 1. Structure of a photocatalyst with the semiconductor in orange and the cocatalysts in grey. Valence and conduction bands of the semiconductor are in red and blue, respectively.

The photocatalytic reaction can be divided into several sequential processes (Figure 1). The efficiency of these steps is mainly governed by the properties of the semiconductor, the cocatalyst or the interface between the two. Successful photoelectrocatalysis proceeds via the following six steps.

Step 1 corresponds to the light absorption by the semiconductor creating an electron (e^-) and hole (h^+) pair, called exciton.[52] The light absorption is mainly governed by the bandgap ($\mathbf{E_g}$) in a semiconductor that can be seen as the difference in energy between the top

of the valence band and the bottom of the conduction band. In short, the bandgap must be low enough to absorb the largest number of photons contained in sunlight and large enough to produce electrons and holes having sufficient energies to perform the two half-reactions. For water splitting reaction, the thermodynamic potential difference is 1.23 eV. In reality, it has been shown that to take into account the unavoidable energy loss due to all the electron transfers and entropic loss,[53,54] the bandgap of the semiconductor is required to be above 1.8 eV or, more ideally, between 2.0 and 2.5 eV (to maximize the attainable efficiencies with some variations).[44,55–57] Figure 2(a)-(c) presents the variation of the solar to hydrogen (STH) efficiency as a function of the bandgap of the semiconductor, along with the classical Shockley-Queisser limit of a photovoltaic device based on a p-n junction.[44,58] This simulation includes some models of the energetic losses, including overpotentials for the half-reactions.[44] It is interesting to see the large difference between the theoretical maximum photoconversion efficiencies between a standard p-n junction photovoltaic cell (around 35 %; power efficiency) and the maximum STH efficiency (around 12%; energy efficiency based on bandgap energy and hydrogen product energy) using a single photocatalyst. Because a single semiconductor based photocatalyst has a limited attainable efficiency, multiple semiconductor configurations are considered, such as Z-scheme structures or so-called type-II heterostructure.[59–62] One of the driving forces motivating the development of such architecture is the possibility to achieve, in principle, much higher attainable efficiencies (Figure 2(b)-(d)).[44,56] The maximum attainable STH energy efficiency using two-semiconductor-based materials is ~25% when a tandem configuration is used together with highly efficient electrocatalysts.

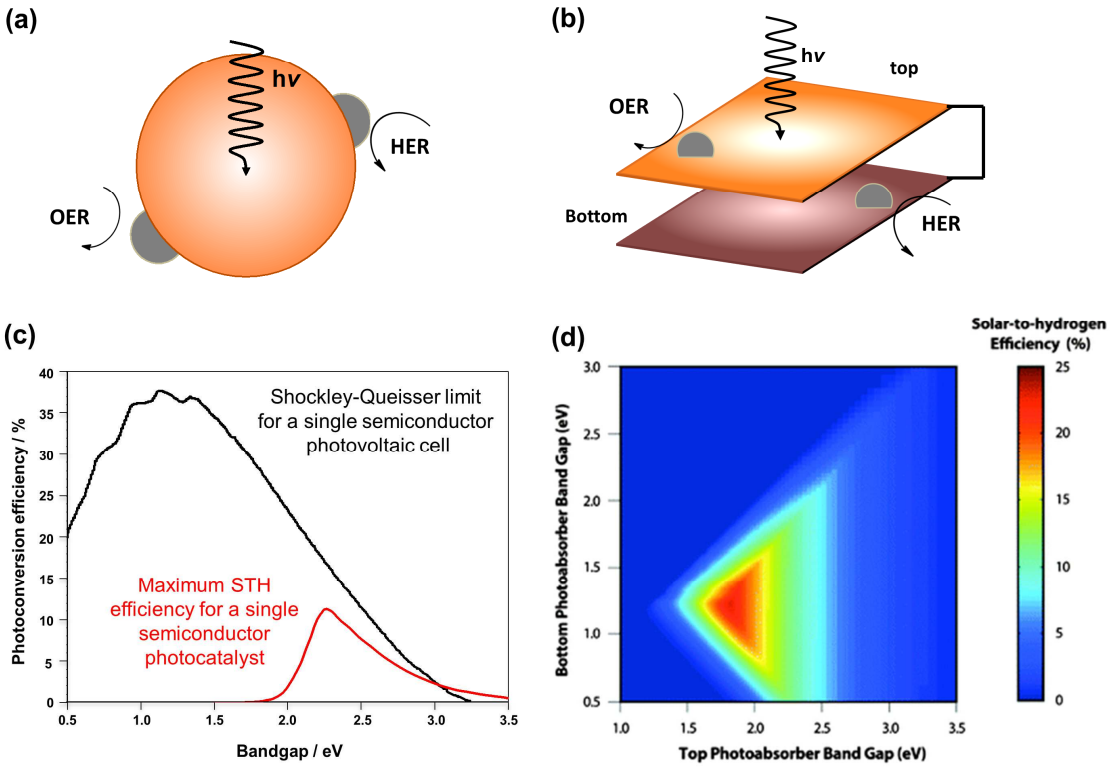

Figure 2. (a) Single semiconductor photocatalyst architecture used for the STH efficiency simulation of (c). (b) Tandem cell architecture used to perform the simulation of the STH efficiency of (d). (c) Comparison between the Schockley-Queisser limit of a photovoltaic cell and the Solar-to-Hydrogen (STH) efficiency of photocatalysts as a function of the bandgap of the semiconductor. (d) STH efficiency of two-junction photocatalysts as a function of the bandgaps of the two semiconductors. Figure reprinted with permission from "B.A. Pinaud et al. Energy Environ. Sci. 2013, 6, 1983" with the permission of the royal society of chemistry.

Step 2: The exciton dissociation. After light absorption, the electron and the hole are bound, creating a particle called an exciton. The electron and the hole must be separated to perform the redox reactions. The exciton ionization energy is called exciton binding energy, noted E_b. To have free charge carriers, this energy should be lower than the thermal energy (~25 meV at room temperature).[63] If the exciton is not dissociated, it will quickly recombine, losing the energy of the photon. The exciton binding energy is mainly governed by the dielectric constant of the material, noted ε_r. The dielectric constant represents the

ability of the material to screen charges. The larger the dielectric constant, the easier it will be to dissociate the exciton. In fact, materials frequently used in photovoltaics (e.g., Si, CdTe, GaAs) have a dielectric constant higher than 10, and their E_b is always lower than 25 meV.[64] This value of 10 for ε_r can be seen as a target to develop new semiconductors for water splitting.

Step 3: Charge carrier diffusion. Once the exciton is dissociated, electrons and holes diffuse to the surface, according to semiconductors physics.[65] This diffusion is characterized by the diffusion coefficient, D, of the charges related to the charge carrier mobilities, μ, by the Einstein relationship (equation (3)). The mobility is linked to the effective masses, m^*, and the collision time, τ (equation (4)).

$$D = \frac{k_B T}{e} \mu \quad (3)$$

$$\mu = e \frac{\tau}{m^*} \quad (4)$$

There is no fundamental lower limit for the value of the charge carrier mobilities or effective masses. But empirically, by analyzing all semiconductors efficient for photovoltaic applications, it appears that they all have a mobility higher than 10 $cm^2\ s^{-1}\ V^{-1}$ and an effective mass lower than 0.5 electron mass at least in one crystallographic direction. Based on this empirical observation, all semiconductors having an effective mass lower than 0.5 electron mass (9.1×10^{-31} kg, noted m_0 hereafter) for holes and electrons can be considered as having good charge carrier mobilities.

Step 4: Charge transfer. In practice, the semiconductors developed to efficiently generated charge carriers are not necessarily adapted to catalyze the two-half reactions of water splitting. In other words, the activation energy or the overpotential of the electrocatalytic reactions are generally large on the surface of the semiconductor. This is the reason why the semiconductor surface is often decorated by cocatalysts having better catalytic

activity toward the electrochemical reactions. The electron or hole transfer must be efficient to have a maximum of charges collected by the cocatalysts. This step depends on the quality of the interface between the cocatalyst and the semiconductor.

Step 5: The electrochemical redox reactions. For water splitting, the electrocatalytic reactions are HER and OER, both of which require multiple electrons (see equations (1) and (2)). The potentials used to split water in photocatalysis come from the charge dynamics inside the semiconductor. In other words, photocatalytic water splitting can be seen as electrocatalytic water splitting, in which the applied potential is not chosen by an external electric circuit as in conventional electrolyzer but depends on the efficiency of the semiconductor to generate a charge flow to the surface as a consequence of steps 1–4 (see above). The efficiency of this step is mainly governed by the overpotential (noted η) associated with the cocatalyst. The overpotential corresponds to the extra energy (or the extra potential) needed to perform one half-reaction beyond the thermodynamic limit. We chose photoelectrochemical performance as an example to show how electrocatalytic performance might influence the case of a photoanode for oxygen evolution reaction, as presented in Figure 3.[66]

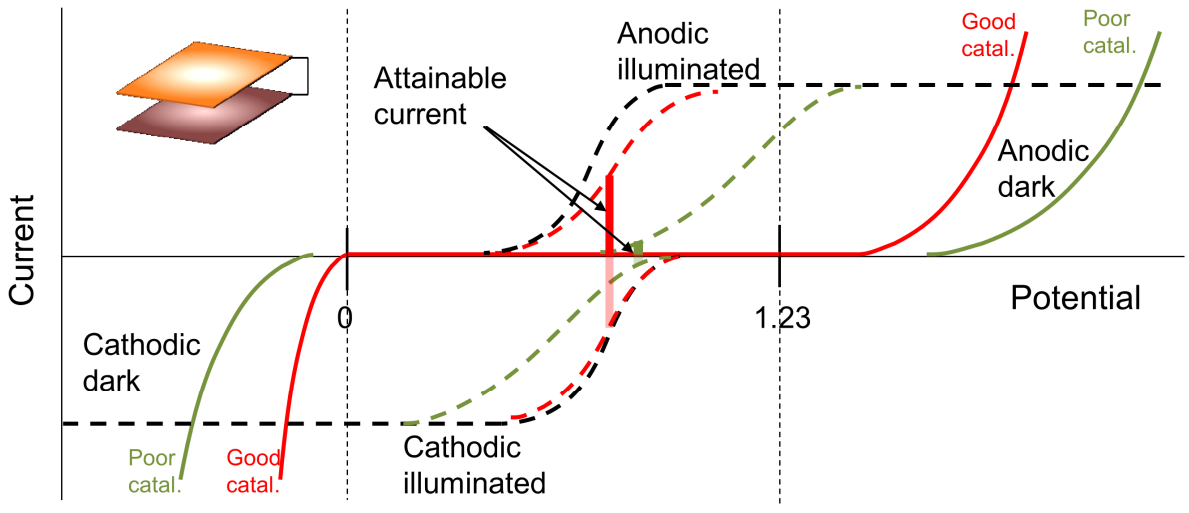

Figure 3. Conceptual schemes representing attainable current as a function of potential in a two-photoelectrode configuration. The same cathodic and anodic currents achieved by the respective photocathode and photoanode will be the total current generated by the entire device. Two types of electrocatalysts (cocatalysts) are arbitrarily chosen to represent their excellent and poor performances. Black dotted lines represent potentially-achievable photoelectrochemical performance from only charge separation, and red and green dotted lines are actual performance obtainable with excellent and poor electrocatalysis.

Step 6: Fluid mechanics and diffusion of ions and molecules. This step presents phenomena happening mainly inside the electrolyte, where the reactions take place.[67] This is an important aspect in the working principle of a water-splitting device, and further improvements of the photocatalytic efficiencies could be obtained by a smart design of the electrolyte. The optimization of the electrolyte at near-neutral pH was reviewed elsewhere.[68]

Development of new semiconductors and photocatalysts (i.e., semiconductor and cocatalyst) fulfilling this list of requirements has been a major source of work for the photoelectrochemistry community, starting from oxides[69–73] but quickly progressing to more sophisticated materials, such as sulfides[70,74–76], oxysulfides[77–80], nitrides[81–84], and oxynitrides.[62,85–87] These new systems are frequently the subject of reviews, highlighting the wealth of new semiconductors designed for photoelectrocatalysis.[16,55,82,88] In parallel, the tools developed by quantum chemists are ever more frequently used to investigate photocatalyst properties,[89–93] mainly based on the Density Functional Theory (DFT).[94] However, rationalizing the differences in activity of these semiconductors is difficult, mainly because of the lack of facile experimental characterization of their optoelectronic properties.

The current review article is dedicated to the characterization of semiconductors, which can be coherently achieved both experimentally and computationally. To make this contribution unique, we focus on the characterizations of optoelectronic properties that can be

directly related to the electronic structures of semiconductor solids. We will present the different techniques available to measure and compute the following key properties, all directly involved from Step 1 to Step 4 (Figure 1).

I. Bandgaps and absorption coefficient. 12
II. Dielectric constant. 25
III. Charge transport properties 29
IV. Exciton binding energy. 37
V. Band positions. 42

I. Bandgaps and absorption coefficient.

The bandgap, E_g, is an essential property of semiconductors, and many publications presenting new semiconductors predominantly focus on reporting E_g to characterize their electronic structures. E_g is an important property since the primary attainable efficiency of a photocatalytic device from photon absorption is directly related to this value (Figure 2). However, the definition of E_g is ambiguous and controversial, sometimes leading to confusion between the optical gap, electronic gap, and HOMO-LUMO gap. A recent article dedicated to the comparison between the different types of bandgaps has been discussed by Breda (Figure 4).[95] Based on this work, we can define the fundamental gap corresponding to the difference in energy between the first ionization potential (IP) and the first electron affinity (EA).

$$E_g\left(\text{fund}\right) = \text{EA} - \text{IP} \tag{5}$$

We can also define the optical gap, corresponding to the energy of transition between the ground state (noted S_0) and the first excited state (noted S_1). This fundamental gap is larger than the optical gap, measured by absorption spectroscopy or photoluminescence. The energy difference between these two gaps originates from the formation of an exciton for optical measurements. The exciton formation energy is noted as E_b.

$$E_g\left(\text{opt}\right) = \text{EA} - \text{IP} - E_b \tag{6}$$

E_b is generally relatively small for standard covalent semiconductors (few dozens of meV) when compared to the fundamental bandgap (few eV). Thus, in general, E_g(fund) and E_g(opt) are very close.

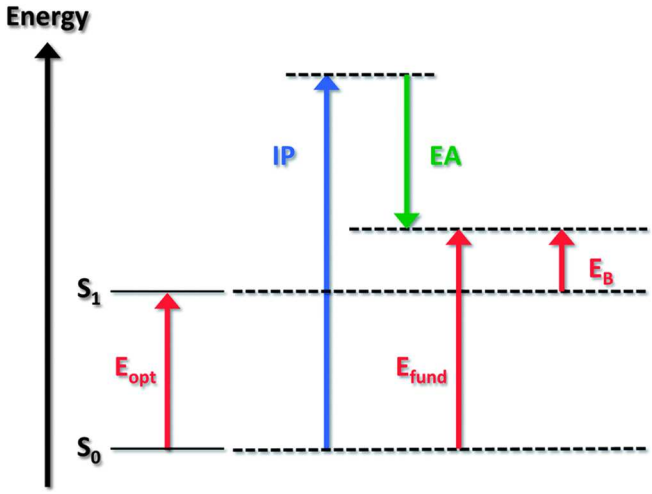

Figure 4. An energetic diagram presenting the different bandgap and their relationships. E_B in this figure corresponds to E_b in the text. Figure reprinted with permission from "J.-L. Breda Mater. Horiz. 2014, 1, 17-19" with the permission of the royal society of chemistry.[95]

Finally, we can define the bandgap corresponding to the energy difference between the top of the valence band (noted ε_{VB}) and the bottom of the conduction band (noted ε_{CB}). By analogy to molecular calculations, one can call this bandgap the HOMO-LUMO bandgap or the mono-electronic bandgap.

$$E_g(\text{mono}) = \varepsilon_{CB} - \varepsilon_{VB} \quad (7)$$

These energies are obtained by self-consistently solving the monoelectronic Kohn-Sham equations. Removing or adding an electron to a system, with the associate energies IP and EA, change all the electronic structure of the system because the electrons interact with each other leading to orbital energies variation after the electron addition/removal. Thus, to compute IP and EA, the full electronic structure relaxation induced the change in the number of electrons must be taken into account, that is time consuming to compute or even impossible for periodic system (this aspect is discussed later in the manuscript). In 1934, Koopman demonstrated that under the assumption that if the orbital relaxation is not important under electron addition/removal or in other words if the orbitals does not change in energy and in shape, the orbital energies correspond to IP and EA ($IP \approx -\varepsilon_{HOMO}$ and $EA \approx \varepsilon_{LUMO}$).[96] This

is called the Koopman's theorem and is the most frequent assumption used to estimate IP and EA of a system. This theorem was demonstrated in the framework of Hartree-Fock theory.[96] An attempt to adapt this theorem to DFT was performed by Janak in 1978.[97] The application area of Janak's theorem is smaller, because this theorem works only for the HOMO orbital (i.e., IP $\approx -\varepsilon_{\mathrm{HOMO}}$). Nevertheless, the community has taken the habit to apply the Koopman's theorem to DFT allowing to estimate the EA from the LUMO energy or in some scientific fields to use core orbitals to estimate core level energies.

$$E_{\mathrm{g}}\left(\mathrm{fund}\right) = \mathrm{EA} - \mathrm{IP} \approx \varepsilon_{\mathrm{CB}} - \varepsilon_{\mathrm{VB}} = E_{\mathrm{g}}\left(\mathrm{mono}\right) \tag{8}$$

This assumption is very rough for molecules but works relatively well (for the precision we are looking for) for solids, which will be discussed later.[98] Because the exciton binding energy usually requires only a small correction to go from the fundamental bandgap to the optical bandgap, the monoelectronic bandgap is usually directly compared to the optical bandgap.

Benchmarks of DFT functionals to simulate E_{g}(mono), thus by using the top of the valence band and the bottom of conduction band energies, have been the subject of numerous works in the literature.[99–108] As a matter of fact, some of us presented a benchmark focused on semiconductors used in photoelectrocatalysis and photovoltaic, using functionals frequently used in solid-state chemistry to computed electronic structures: PBE[109] (GGA), B3LYP (global hybrid, 20% of exact exchange), PBE0[110] (global hybrid, 25% of exact exchange) and HSE06[111,112] (range-separated hybrid). The results of this are presented in Figure 5.[63]

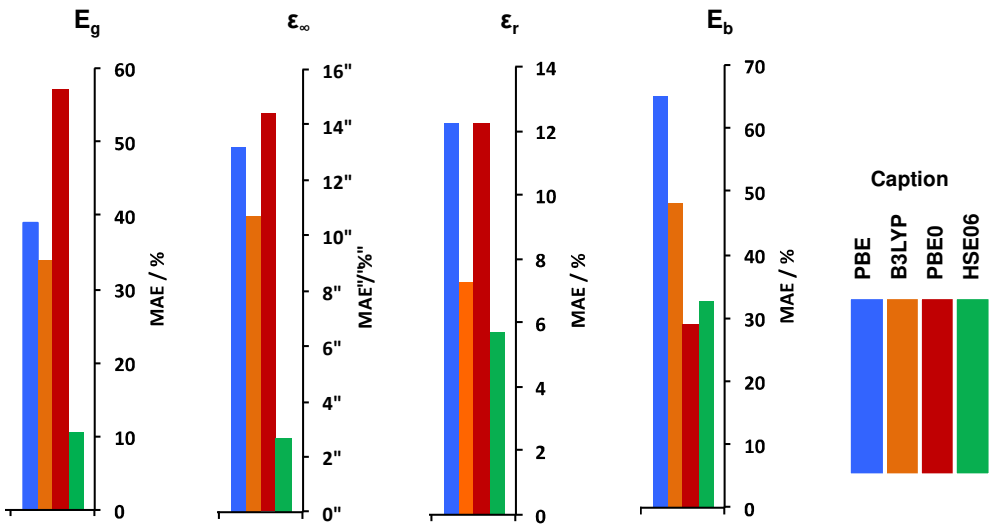

Figure 5. Mean absolute error (MAE) of the four investigated functionals on the selected properties. MAE is obtained by performing the arithmetic average of the absolute error (compared to experiment). Adapted with permission from "Le Bahers, T.; Rérat, M.; Sautet, P. *J. Phys. Chem. C* 2014, *118*, 5997". Copyright (2018) American Chemical Society.[63]

If we focus on the bandgap calculation, GGA and global hybrids give bandgaps with a relatively large error. Actually, GGA strongly underestimates bandgaps while global hybrids overestimate it.[104] The range-separated hybrid HSE06 gives bandgaps with 10% of error. It is interesting to focus on this functional and attempt to understand its reliability. This is a range-separated hybrid, meaning that the exact exchange (or Hartree-Fock (HF) exchange) depends on the interelectronic distance in the evaluation of the exchange integrals, unlike for global hybrids, such as PBE0 and B3LYP functionals, whose exact exchange is constant (Figure 6). Contrary to the well-known range-separated hybrids, such as cam-B3LYP,[113] designed to increase the HF exchange when increasing the interelectronic distance, the HSE06 functional decreases this fraction (Figure 6). The reason for this behavior is practical rather than physical. Decreasing the HF exchange with the interelectronic distance allows reducing the number of exchange integrals to compute on long-range that save a large amount of computational time in solid-state calculation.[111] The parameters governing the variation of HF exchange were fitted to reproduce the bandgap of several semiconductors.[111] HSE06

works well because it is designed specifically for that purpose. Hybrid functionals are frequently considered to be prohibitive in term of computational time, but their implementation in localized basis set (such as Gaussian basis set) codes offers very accurate performances[114], and they can be easily applied to very large systems (up to several hundreds of atoms).[115,116]

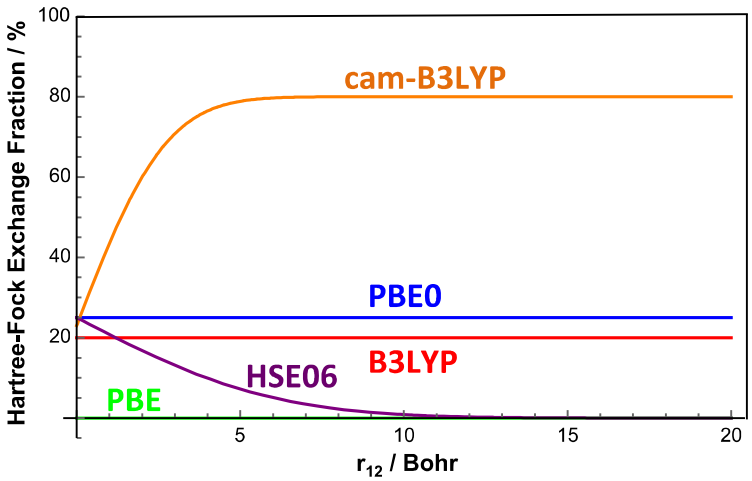

Figure 6. The fraction of exact exchange as a function of the interelectronic distance for several functionals.

It is interesting to note the high reliability of DFT for bandgap simulation based on band (i.e., orbital) energies. In the molecular case, it is well-documented that to take the HOMO-LUMO gap to simulate the first optical transition is a very bad approximation, with errors of several eV.[117] One reason for this is the large exciton binding energy for molecules because of its very localized nature, unlike the case of the solids. Nevertheless, the HOMO-LUMO gap also fails to reproduce the fundamental gap for molecules. This discrepancy comes from the large orbital relaxation induced by electron addition/removal in molecules, making Koopmans's theorem not applicable. The review proposed by Blase *et al.* on that topic is particularly interesting.[117] For solids, this orbital relaxation is very moderate because of the periodic nature of the system. Adding or removing one electron creates an extra charge (electron or hole) delocalized on several unit cells, thus with a diluted influence on the other electrons of these unit cells leading to a moderate orbital relaxation and

making the Koopmans's theorem more applicable. Interested readers are invited to refer to the work published on that topic by Perdew et al.[98] In addition to the fact that the exciton binding energy is generally a weak correction, the monoelectronic bandgap in solid-state systems is generally close to the fundamental and optical bandgaps.

The development of new functionals for solid-state simulation and, more precisely for semiconductor properties calculations, is still a topic of research. One approach proposed is to use global hybrid functionals, but changing the HF fraction for each semiconductor. A first attempt is to assume that a good HF fraction is equal to $1/\varepsilon_\infty$.[103,108,118–122] A less empirical approach is to use the Green-Screened Coulomb interaction formalism (better known as GW) and to extract an HF exchange ratio using a screened exchange operator, as proposed by Galli and coworkers, which can also be adapted to build range-separated hybrid functionals.[123,124] The use of tuned hybrid functionals, based on dielectric constant, works relatively well, leading to errors on the bandgaps below 10%, but has the main drawback of requiring a change of functional when going from one semiconductor to another. New functionals are sometimes presented with superior performance than HSE06.[124,125] Meta-GGA functionals, such as the one developed by Becke and Johnson (mBJ)[101,126] and Verna and Truhlar (HLE17)[125], can also lead to errors around or even below 10%. These functionals are pure functionals, meaning that there is no exact exchange calculation. The consequence is faster calculations compared to hybrid functionals, giving an advantage compared to HSE06 for similar reliability. Unfortunately, the SCF convergence of meta-GGA for some systems and surfaces is sometimes difficult.[127–129]

The good performance assessed of density functionals presented above is valid only for semiconductors based on filled (d^{10}) or empty (d^0) d-shells elements. In general, all the density functionals fail to reproduce the bandgap and electronic properties of semiconductors containing partially filled d-orbitals.[130–136] This is particularly true for the third-row

transition metals. The reason is the strong electronic correlations between electrons of d-shells not properly described by DFT. Two approaches can be used to overcome this important difficulty. The first consists of forcing (artificially) the correlation in the DFT Hamiltonian by adding a phenomenological term, called the Hubbard term.[137–140] Once added, the total energy of the system is given by Formula 9, where U is called the Hubbard parameter, J the screened Stoner-like exchange parameter, and ρ^{σ} is the density matrix.

$$E_{\mathrm{DFT+U}} = E_{\mathrm{DFT}} + \frac{U-J}{2}\sum_{\sigma} Tr\left[\rho^{\sigma} - \rho^{\sigma}\rho^{\sigma}\right] \quad (9)$$

This term promotes the localization of the electrons on d-orbitals inducing a larger correlation. Nevertheless, the strength of this localization is parameterized, corresponding to the U value in Equation 9. This parameter can be adapted, such as reproducing property of the system (bandgap, ionization potential, and atomization energy). As a matter of illustration, Figure 7 presents the influence of the U parameter on the computed bandgap of TiO_2 (anatase and rutile) and compares these values to experimental and HSE06-computed values.[141] The strength of this approach is the speed of calculation, which is close to that of GGA functionals. The weakness is the parameterized character of the approach, making the results parameter dependent. Nevertheless, this approach, due to its easiness of application, is the most used for strongly correlated systems.[130,132,133,137–139,141–143]

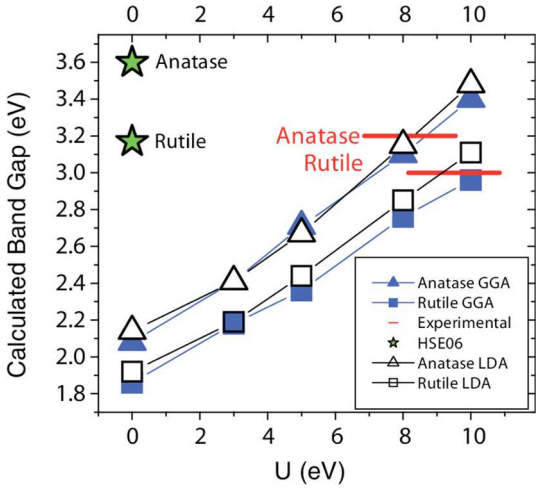

Figure 7. Illustration of the Hubbard Hamiltonian of the bandgap of TiO_2 (anatase and rutile). Figure reprinted with permission from "M.E. Arroyo-de Dompablo *et al. J. Chem. Phys.* 2011, *135*, 054503". Copyright (2018) The American Physical Society.

The most elegant way to improve the description of correlation by DFT is to go beyond the approximations done by DFT in a rigorous manner. Several approaches have been developed in that direction, but the GW approach is mostly used in solid-state chemistry.[99,117,138,144–148] GW is sometimes presented as a "post-DFT" approach. Presenting the full equations of the GW theory goes beyond the topic of this review, and interested readers are invited to look at specific publications.[117,149] The GW method involves two non-local operators called Green's function (G) and the screened Coulomb repulsion (W). Briefly, the GW approach uses orbitals previously obtained by a DFT calculation and performs either a single point calculation (called G_0W_0) or a self-consistent calculation (called scGW). There are several types of "flavors" of GW calculations depending on the level of self-consistency. Finally, the GW calculation gives new energy levels exactly corresponding to the ones measured experimentally by photoelectron spectroscopy.[117] In other words, the GW bandgap should correspond to E_g(fund) (equation 5). In practice, GW calculations are notably more computational resource demanding than DFT. GW provides very accurate bandgaps for d^0 and d^{10} materials, with the same accuracy as for good DFT functionals (see Figure 8).[99,119,150,151] For partially occupied d-orbitals based-semiconductors, GW leads to much more accurate bandgaps than DFT.[132][135] Interestingly, GW methods are increasingly available in quantum chemistry codes. While these are an improvement compared to DFT calculations, the large computational resources needed to perform such calculations prevents their use in large systems.

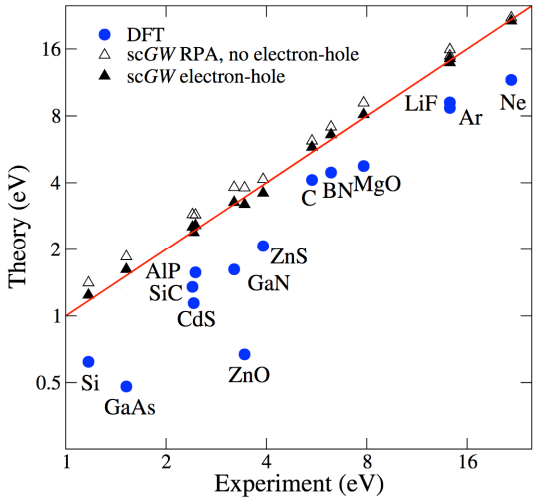

Figure 8. Comparison between DFT (PBE GGA Functional) and GW bandgaps for selected semiconductors. Figure reprinted with permission from [M. Shishkin *et al. Phys. Rev. Lett.* 2007, *99*, 246403]. Copyright (2018) The American Physical Society.[95]

From the knowledge of monoelectronic energies and associated orbitals, whether they come from DFT or GW calculations, the imaginary part of the frequency dependent dielectric constant can be computed based on band-to-band transitions using the formula (10)-(12).[152] From this formula, it appears that only the transitions at the same *k*-point (vertical transition in the band structure) are taken into account. In other words, indirect transitions are not considered by this approach. Finally, the real part of the dielectric constant is computed from the imaginary part, using the Kramers-Kronig transformation (formula (12)) and the absorption coefficient is computed from the real and imaginary part of the dielectric constant (formula (13)-(14)). This approach is now frequently used to evaluate the absorption spectra of semiconductors.[87,152–160] This works fairly well if (i) the methodology used to compute the electronic structure gives a reasonable bandgap and (ii) the monoelectronic approach is a good approximation of the electronic structure.

$$\varepsilon(\omega) = \varepsilon^{(1)}(\omega) + i\varepsilon^{(2)}(\omega) \tag{10}$$

$$\varepsilon^{(2)}_{\alpha\beta}(\omega) = \frac{4\pi e^2}{\Omega} \lim_{q\to 0} \frac{1}{q^2} \sum_{v,c,k} 2w_k \delta(\dot{o}_{ck} - \dot{o}_{vk} - \omega) \left\langle u_{ck+qe_\alpha} \middle| u_{vk} \right\rangle \left\langle u_{vk} \middle| u_{ck+qe_\beta} \right\rangle \tag{11}$$

$$\varepsilon_{\alpha\beta}^{(1)}(\omega) = 1 + \frac{2}{\pi}\int_0^{\infty} \frac{\varepsilon_{\alpha\beta}^{(2)}(\omega')\omega'}{\omega'^2 - \omega^2} d\omega' \quad (12)$$

$$\kappa_{\alpha\beta}(\omega) = \sqrt{\frac{\sqrt{\varepsilon_{\alpha\beta}^{(1)}(\omega)^2 + \varepsilon_{\alpha\beta}^{(2)}(\omega)^2} - \varepsilon_{\alpha\beta}^{(1)}(\omega)}{2}} \quad (13)$$

$$\alpha_{\alpha\beta}(\omega) = \frac{4\pi}{\lambda}\kappa_{\alpha\beta}(\omega) \quad (14)$$

The community of computational solid-state chemistry is also working on the implementation of TD-DFT that would give access to a much more accurate simulation of the frequency-dependent dielectric constant, and ultimately a more accurate absorption coefficient (Figure 9).[161–163]

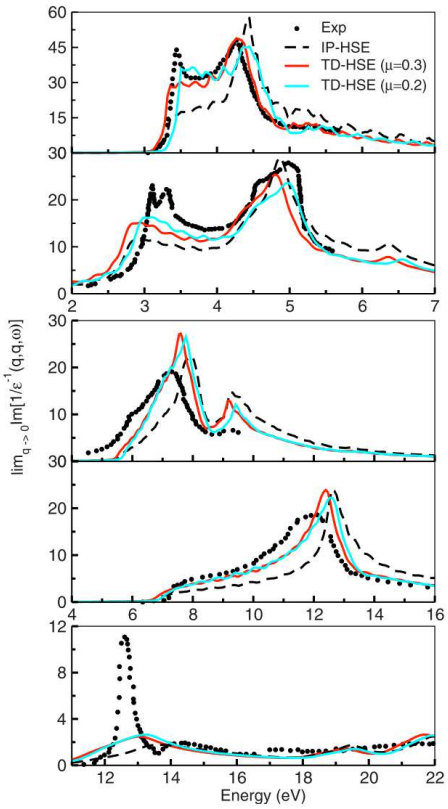

Figure 9. Example of a simulation of the imaginary part of the dielectric constant by TD-DFT for Si, GaAs, SiC, C, and LiF from top to bottom respectively. Figure reprinted with permission from [J. Paier *et al. Phys. Rev.B* 2008, *78*, 121201].

While bandgap energy is directly associated with the maximum attainable efficiency of the photoelectrocatalysis, the most beneficial property involved in photon absorption is the absorption coefficient as a function of wavelength. UV-visible spectroscopy is a direct method used to determine this property.[164] Based on the Beer-Lambert law, the light intensity $I(x)$ as a function of the point x from the surface to the bulk, which has a dimensionality of power (or photon numbers) per area (e.g., W m^{-2} or photons m^{-2}), is defined as

$$I(x) = I_0 \exp(-\alpha x) \tag{15}$$

where α is the absorption coefficient, which has a dimensionality of inverse length (e.g., cm^{-1}). This exponential decay of light intensity is no longer true if non-linear phenomena happen (multi-photon absorption). At the typical light intensities used to perform the measurement, however, these non-linear phenomena are extremely uncommon and can be ignored in the analysis. Because of this proportionality coefficient, it is convenient to describe the absorption measurement with dimensionless values, such as absorptance, a, and transmittance, T, which are the relative amount of the light being absorbed by, and passing through the sample, respectively, with a thickness, l. In the ideal case where the incident light contributes solely to absorption with the material, the absorptance can be described as;

$$a = \frac{I_{in} - I_{out}}{I_{in}} = 1 - T = 1 - e^{-\alpha l} \tag{16}$$

The reciprocal of absorption coefficient gives absorption depth (i.e., the thickness of the semiconductor requiring sufficient number of photons at a given wavelength). In reality, however, the incident photons might be lost by additional processes, such as specularly reflected (R_s), forward-scattered (S), and back-scattered (R_d),[164] and thus;

$$a + T + R_s + S + R_d = 1 \tag{17}$$

The frequently used dimensionless parameter, the absorbance, A, should not be confused with these values, which is defined as:

$$\alpha = 1 - 10^{-A} \tag{18}$$

For a given semiconductor, it is useful to obtain the absorption coefficient as a function of incident wavelength. A thin-film configuration of the bulk semiconductor that minimizes the contribution of scattering is The measurement becomes more accurate if a thin film with absolute thickness is defined. Swanepoel proposed a useful method to determine film thickness using interference fringes of the transmittance spectrum[165]. In a transmittance mode,[166] the complete light absorption should be avoided to extract the information of α. It is, therefore, necessary to fabricate reliable and sufficiently-thin films that reflect the characteristics of the solid (i.e., the same displacement of atoms as the bulk solid). In practice, it is conducted to measure the absorption coefficient focusing on two measured parameters, which are transmittance, T, and reflectance, R,[167] by minimizing other contributions such as scattering. When the reflectance is small, the absorption coefficient is reported using the following relationship[168].

$$\alpha = -\frac{1}{d}\ln\frac{T}{(1-R)^2} \tag{19}$$

It is important to give extra attention to the type of substrates used in the absorption measurement because it is known to drastically affect the obtained properties.[169]

The common approach to measure absorption characteristics of powder semiconductor materials is diffuse reflectance measurement. Use of an integrating sphere to collect all the scattered light is effective at improving the accuracy of the measurement. The Kubelka-Munk model is based on the measurement assuming scattering and absorption, the relationship of which is given by[170,171];

$$f(R) = \frac{(1-R)^2}{2R} = \frac{\alpha}{s} \tag{20}$$

The Kubelka-Munk function is theoretically proportional to the absorption coefficient, as can be seen in Equation (20). The bandgap is thus obtained using this relationship, even if the scattering coefficient *s* is unknown. However, Murphy discussed uncertainty to determine bandgap using the Kubelka-Munk function, especially for doped semiconductors[172]. The weak part of the absorption spectrum is frequently overestimated. According to Murphy, the absorption coefficient due to doped electronic state is so weak that the contribution to photoelectrocatalysis using this transition is expected to be minimal[172]. Also, it is important to analyze the data with zero absorption background beyond the bandgaps as this would provide important information about the dopants and defects [173].

Using the obtained absorption coefficient, the bandgap is commonly determined using the Tauc plots. The Tauc relationship[174], which is supported by Davis and Mott[175], provides the following relationship when the reasonable absorption is achieved, typically $\alpha > 10^4$ cm^{-1};

$$\alpha h\nu \propto \left(h\nu - E_g\right)^{\frac{1}{n}} \tag{21}$$

where *n* can take values of 3, 2, 3/2, or 1/2, corresponding to indirect (forbidden), indirect (allowed), direct (forbidden), and direct (allowed) transitions, respectively[164,176,177] The nature of the bandgap (direct, indirect…) is generally obtained from DFT calculations of band structures. Tauc plots, i.e., $(\alpha h\nu)^n$ as a function of $h\nu$ (*n* is the same as above) give E_g from the intersection of a line tangent to the slope in the linear region of the absorption onset with the baseline (Figure 10). [164,176,177] Bandgaps of many semiconductors are compiled in ref.[64]

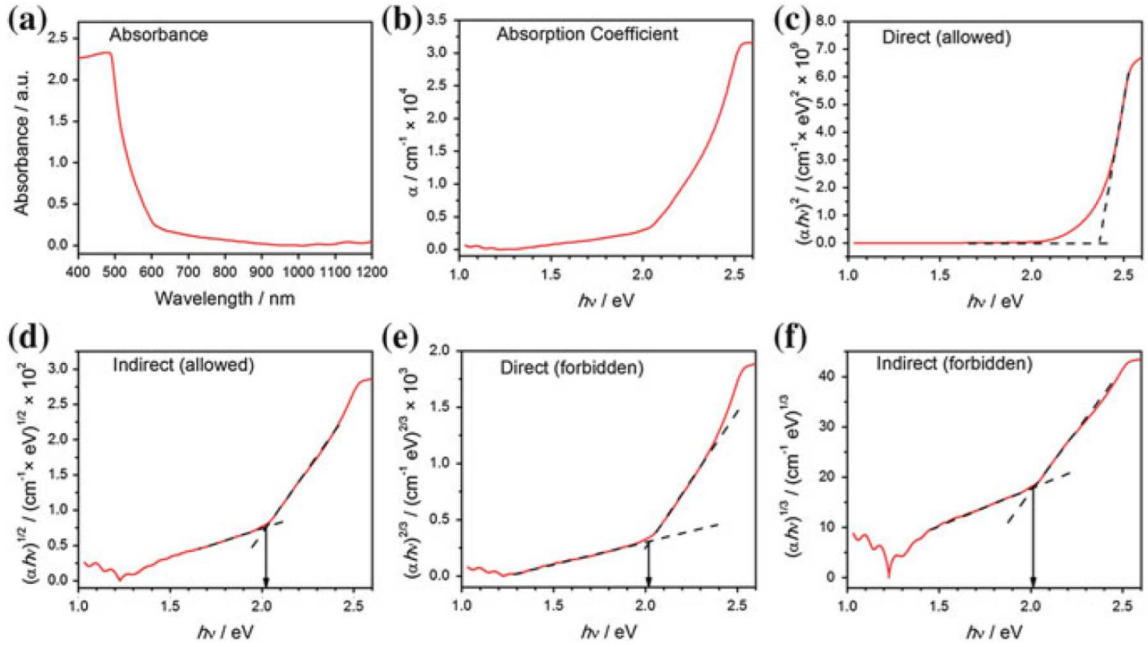

Figure 10. Absorption spectra of Cu_2O (a) along with the related absorption coefficient (b) and several ways to determine the bandgap from the Tauc plot, assuming direct-indirect/allowed-forbidden transitions (c)-(f). Figure reprinted with permission from [Z. Chen et al. Photoelectrochemical Water Splitting, 2013, Springer-Verlag New-York]. Copyright (2018) Springer-Verlag New-York.

Photoluminescence spectroscopy is another experimental method to the determine bandgap[178]. In theory, the onset of the luminescence signal should correspond to the bandgap described previously. The intrinsic band structures are reflected by the measurement at low temperatures, avoiding thermal contribution. The bandgap determination by this technique, however, cannot be applied to nonradiative transitions and the samples with indirect bandgap semiconductors. It is also noted that many dopant states appear in the signals and, thus, often lead to ambiguity to determine bandgaps.

II. Dielectric constant.

When an electric field ($\vec{E}$) is applied on a dielectric material, an electric displacement field ($\vec{D}$) appears within it. Both electric fields are linked by the dielectric constant ε_r.

491 $$\vec{D} = \varepsilon_0 \varepsilon_r \vec{E} \quad (22)$$

492 This dielectric constant represents the ability of dielectric material to screen the external
493 electric field by the apparition of a polarization. This polarization comes from the
494 reorganization of the electron density or the motion of the ions constituting the material. The
495 dielectric constant induced by the electron density is named ε_∞, and the contribution of the
496 dielectric constant involving the ionic motions is noted ε_{vib}. Finally, we have:

497 $$\varepsilon_r = \varepsilon_\infty + \varepsilon_{vib} \quad (23)$$

498 A study on dielectric materials itself is an important field. The dielectric constants of
499 various materials are compiled elsewhere.[64,179,180] There are many ways to
500 experimentally measure the dielectric constant of a semiconductor, and one of the common
501 ways is to conduct capacitance measurements with varied frequency after making a disc
502 device with two metal contacts at each side. For example, dielectric properties of TiO_2
503 powder was measured by making pellets of the sample.[181] For the powder semiconductor,
504 the measurement may give overestimation due to extrinsic microstructural features.[182]
505 Another common technique to measure dielectric properties for powder sample is
506 ellipsometry (Figure 11).[64,183]
507

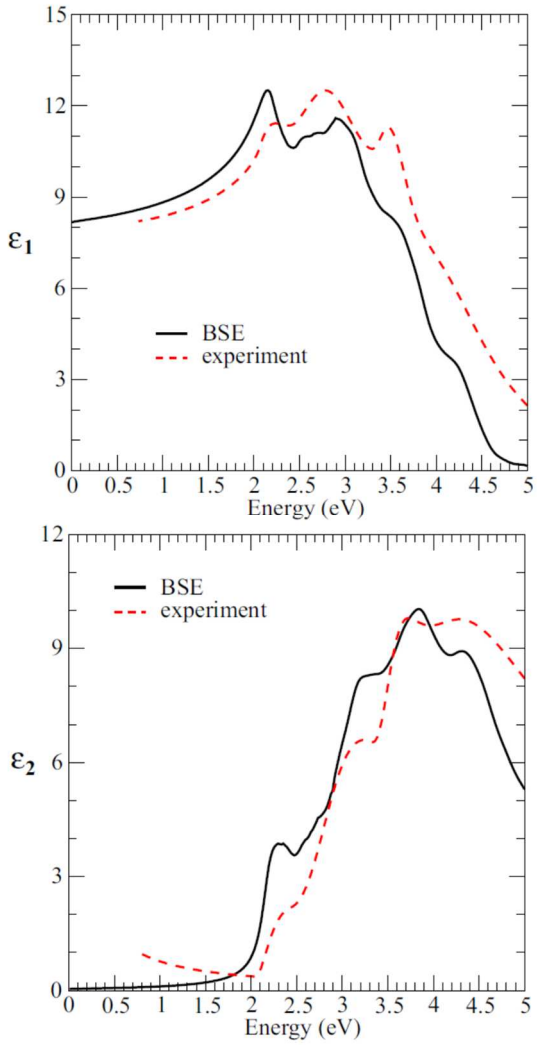

Figure 11. Experimental (obtained by ellipsometry) and computed (GW/BSE) frequency dependent dielectric constant (ε_1 real part and ε_2 imaginary part) of Ta_3N_5. Figure reprinted with permission from [J. Morbec *et al. Phys. Rev. B* 2014, *90*, 1] Copyright (2018) The American Physical Society.

Computationally, the electronic contribution to the static dielectric tensor can be evaluated through a coupled-perturbed Hartree-Fock/Kohn-Sham (CPHF) scheme adapted to periodic systems[124,162,184–186] or by applying an electric field on the system during the SCF procedure[187]. While more time consuming, determining the total dielectric constant by performing SCF calculations with an electric field considers local field effects because of the self-consistent nature of the calculation. Nevertheless, CPHF and electric field approaches usually lead to similar results, but more sensitive on the choice of the functional (for DFT

520 calculation) than the way to compute the electronic contribution to the dielectric constant. The
521 reliability of DFT to compute the electronic contribution to the dielectric constant has been
522 assessed in several publications.[63,161,188–190] Results are typically close to experimental
523 data, and the exchange-correlation functional typically has a weaker effect on the dielectric
524 constant than the for the bandgap. In fact, the standard deviation of the DFT for a series of the
525 semiconductor is given in Figure 5. The standard deviation is below 20% for all functionals. It
526 is important to note that the ordering of functionals for the bandgap simulation is the same for
527 ε_∞. Consequently, range-separated functionals are the best for simulating ε_∞. However, as
528 mentioned above, the choice of the function has, in general, not a large impact on the final
529 dielectric constant. Thus, global hybrid or even GGA can reasonably be used to compute that
530 property.

531 The vibrational contribution is computed from the phonon spectrum, following
532 Formula (24). ν_p is the phonon frequency of mode p, V is the unit cell volume, and Z_p is the
533 mass-weighted mode effective Born vector. The intensity I_p of IR absorbance for a given
534 mode p is proportional to $|Z_p|^2$.[191] From this formula, it appears that the softer the
535 vibrational modes, the more they contribute to the dielectric constant.

536 $$\varepsilon_r = \varepsilon_\infty + \varepsilon_{vib} = \varepsilon_\infty + \frac{4\pi}{V}\sum_p \frac{Z_p^2}{\nu_p^2} \quad (24)$$

537 The agreement between theory and experiment for the vibrational dielectric constant is also
538 very good, whatever the functional chosen (Figure 5). But this conclusion is no longer
539 available for very large dielectric constants (>100). In these cases, the very soft vibrational
540 modes leading to the large dielectric constant are non-harmonic, thus badly reproduced by
541 DFT in the harmonic approximation. For these difficult systems, DFT results are qualitative
542 informing only on the presence of these soft modes.
543

III. Charge transport properties

The electron and hole transport is an important phenomenon, not only in photoelectrocatalysis but also for several other applications, including but not limited to photovoltaic and thermoelectric. In some aspect of semiconductor physics, the charge carrier drift due to an electric field of a space charge zone plays a fundamental role (such in a p-n junction), but as pointed out by Grätzel et al. in nanoparticulate materials with a high density of impurities, the space charge zone plays only a marginal role and charge carrier transport are mainly governed by thermal diffusion.[192–195] To quantify the transport at a first guess, the measurement of the conductivity is considered. This property depends on the charge carrier density n (generally in cm^{-3}), the charge of the charge carrier density q (in C) and the mobility of the charge carrier density μ (in $cm^2\ V^{-1}\ s^{-1}$) as presented in equation (25). In intrinsic (i.e. without any doping) semiconductors in the dark, the conductivity increases with increasing the temperature because of conduction band population with thermal energy (increase of n in equation (25)). But under doping or light exposure, the charge carrier densities (electrons in the conduction band and holes in the valence band) increase from another reason than temperature. This can lead to a different behavior of the conductivity has a function of the temperature. The value of the conductivity is dependent on temperature and purity and synthesis conditions. For that reason, the mobility μ is considered to be a better intrinsic property of the material to quantify the transport of charge carriers.

$$\sigma = nq\mu \tag{25}$$

Furthermore, the conductivity and diffusion coefficient are diretly related (see Equation (4)). Two main theories are used to interpret the transport properties in optoelectronic materials. The first theory is called the band-like mechanism and is related to the curvature of the band-structure leading to the quantity called effective mass. This theory works well for delocalized charge carriers. Thus, this theory is adapted for highly covalent d^0 or d^{10} semiconductors. The

band-like model is sometimes called the rigid band-model. This means that, by applying this model, we assume that the bands or, more generally, the electronic structure is almost unaffected by the electron and hole generation. This is a good approximation if the charge carriers are delocalized on several unit cells, thus having a diluted influence on the ions. For systems having the more localized character of their orbitals, the charge carriers can be centered only on few ions, leading to a large perturbation around these atoms. The main consequence is generally a geometrical relaxation around the atoms, stabilizing the system and increasing the localization of the electron and the hole. The term self-trapping is generally used to name this phenomenon. The particle made of the charge carrier and the geometrical relaxation is called a small polaron.[196] The polaronic conductivity is based on a hopping mechanism, well described by the Marcus theory.[197–199] In this theory, the polaron jumps from one site to another, leading to mobility given by Equation (26).[200]

$$\mu = \frac{eR^2 n}{k_B T} \nu e^{-\frac{Ea}{k_B T}} \quad (26)$$

where R is the distance between the two hopping sites and n is density of hopping sites. This mobility is thermally activated, which increases with increasing the temperature, following an Arrhenius behavior, in contrast to the mobility governed by a band-like mechanism, which decreases with the temperature.[201,202] To determine if the transport mechanism is a band-like mechanism or a polaronic mechanism, the measurement of the mobility as a function of the temperature is generally performed. An increase of mobility as a function of the temperature indicates a thermally activated mechanism, and thus a hopping mechanism for the polaron. A decrease of the mobility with the temperature is more in favor of a band-like mechanism of charge transport, affected by phonons generated by increasing the temperature. This is illustrated in the work by Lee *et al.* on a donor-acceptor type thiophene-thiazole co-polymer thin film, where the nature of the transport mechanism can change from band-like to polaronic depending on the drain field applied on the film (Figure 12). [63]

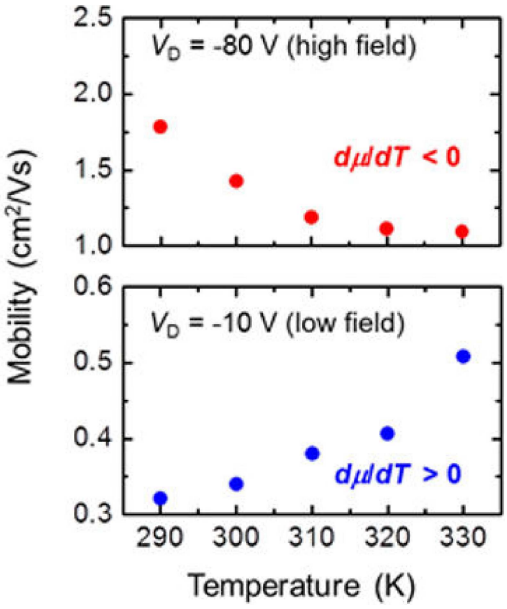

Figure 12. Temperature-dependent mobility as a function of the drain field applied on polymer based on the thiophene-thiazole groups. Adapted with permission from "Lee, J. et al. *J. Am. Chem. Soc.* 2015, *137*, 7990". Copyright (2018) American Chemical Society.[63]

Band-like transport. In the band-like transport theory, the charge carrier mobility is given by the formula (4), including the collision time τ and the effective masses m^*. The concept of effective masses comes from solid-state physics and is related to the curvature of the top of the valence band (for holes) and bottom of the conduction band (for electrons) in the reciprocal space along one direction of the band structure.[39,203–205] The collision time, τ, is extremely experimental dependent and involves all the scattering events (electron-electron, phonon-electron, and electron-impurities) and cannot be easily theoretically evaluated. The effective mass can be obtained by fitting these band extrema by the formula:

$$E(k) = E(k_0) \pm \frac{\hbar^2}{m_{\parallel}^*}(k_0 - k_{\parallel})^2 \pm \frac{\hbar^2}{m_{\perp}^*}(k_0 - k_{\perp})^2 \qquad (27)$$

The ± is + for the conduction band and – for the valence band. k_0 is the vector of the reciprocal space where the band is at its extremum. The symbols $\parallel$ and $\perp$ refer to the longitudinal and perpendicular axes that depend on the structure of the crystal. The effective masses are obtained by fitting the bottom of the conduction band (for the electron effective

mass) and the top of the valence band (for the hole effective mass) with a parabolic function. To calculate the effective mass in that way, the band structure must be computed in several directions. For highly symmetrical crystals, one generally chooses the most symmetric directions. For low symmetry systems, the choice of the crystallographic directions is more difficult and generally arbitrary. Ideally, the effective masses should be computed in a large number of directions to obtain a contour plot allowing to attribute the parallel and perpendicular directions of equation (26), as illustrated in Figure 13 from the work of Feng et al.[206] But, in general, researchers have focused on the simplest directions.

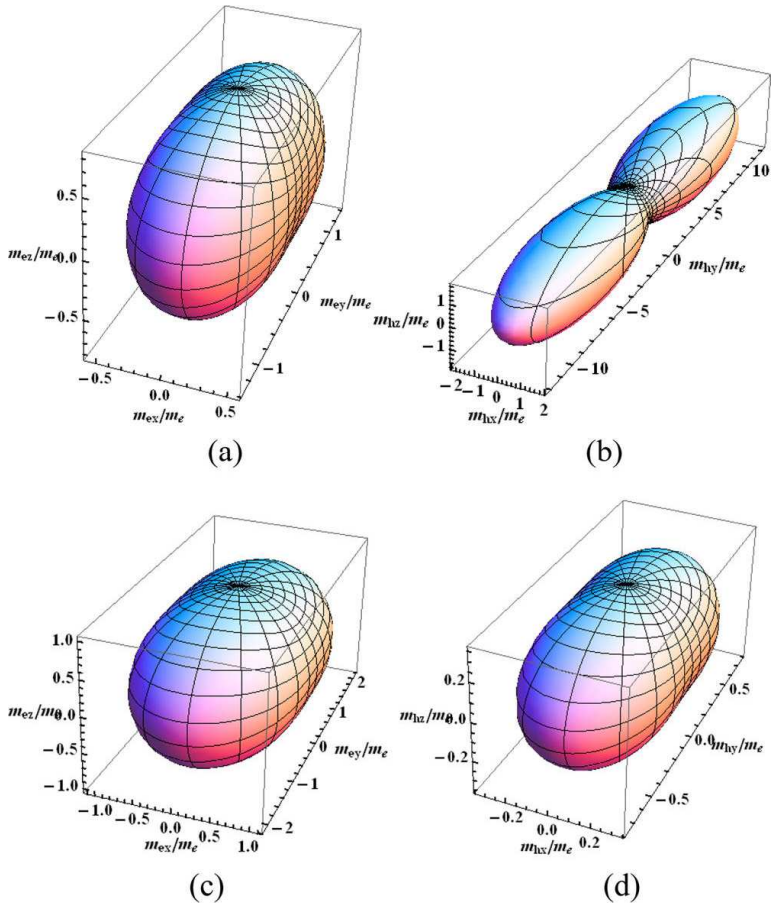

Figure 13. The contour plots of the effective masses of holes and electrons close to the Γ point for $CH_3NH_3PbX_3$ (X = I and Br). (a) m_e* of $CH_3NH_3PbI_3$; (b) m_h* of $CH_3NH_3PbI_3$; (c) m_e* of $CH_3NH_3PbBr_3$; (d) m_h* of $CH_3NH_3PbBr_3$. Figure reprinted with permission from [J. Feng and B. Xiao, J. Phys. Chem. Lett. 2014, 5, 1278-1282]. Copyright (2018) The American Chemical Society.

625 The effective mass calculation from the band-structure is the most frequent approach used by
626 the quantum chemists to characterize the charge carrier
627 mobilities.[63,78,80,154,158,160,207–211] This property can also be used to analyze the
628 excited state entropy of the semiconductor, considered as a source of efficiency decrease, as
629 presented by Osterloh.[53] Assessing the reliability of DFT for that specific property is
630 difficult since we lack experimental data to compare the results. Nevertheless, some classes of
631 semiconductors were deeply characterized leading to the effective mass dataset. Kim *et al.*
632 compared the PBE (GGA), mBJ (meta-GGA), and HSE06 (range-separated hybrid)
633 functionals and found that the non-local nature of the exchange part of HSE06 was necessary
634 to accurately reproduce the effective masses.[212] GW band structures can also be used to
635 evaluate effective masses, typically those close to the masses obtained with hybrid
636 functionals.[150,151,213,214] Beyond the quantitative evaluation of the effective mass, it is
637 important to recall that this property is deeply related to the covalency of the chemical
638 bonds.[204,215,216] Favoring the covalency of the chemical bounds reduces the effective
639 mass and consequently increases the charge carrier mobilities. The covalency can be tuned by
640 changing the chemical nature of the elements or by changing the local geometries, as
641 illustrated by Ha *et al.* for the hole effective mass dominated by the Sn-O interaction in tin
642 oxides (Figure 14).

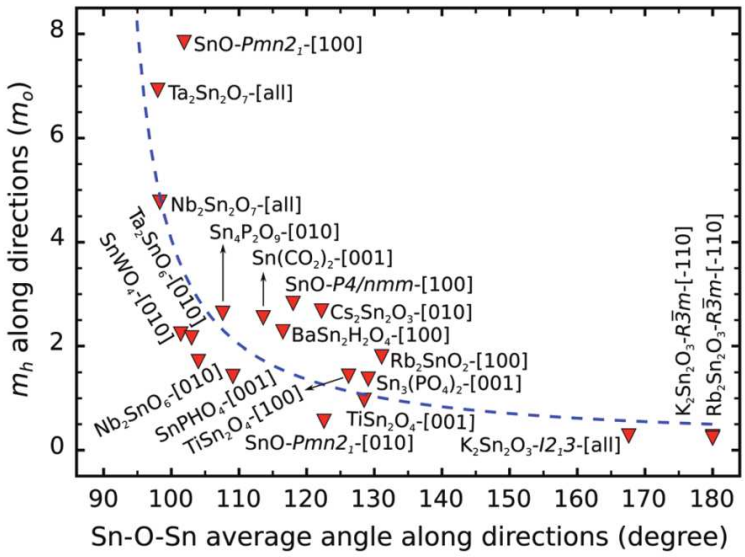

Figure 14. Hole effective mass as a function of the Sn-O-Sn bond in several tin oxides. Figure reprinted with permission from [V.-A. Ha *et al.,* J. Mater. Chem. C. 2017, 5, 5772-5779]. Copyright (2018) The Royal Society of Chemistry.

It is sometimes difficult to find the "good" crystallographic direction for the effective mass calculation, or sometimes, there are several bands extrema close in energy. In these specific cases, the effective masses can be computed using Boltzmann transport theory[217] with the equations (28)-(30), where σ is the conductivity of the material and τ is the collision time. This corresponds to an effective mass averaged on the density of state of the conduction band and the valence band parameterized by the scattering time τ. Using that approach, the calculation of the effective mass is a post-treatment of a full band structure. Several codes now offer the possibility to perform such analysis.[116,217–219]

$$\sigma_{\alpha\beta} = -e^2\tau\sum_i\int v_\alpha(i,k)\,v_\beta(i,k)\frac{\partial}{\partial E}f\left(E(i,k),\mu,T\right)\frac{dk^3}{4\pi^3} \quad (28)$$

$$v_\alpha(i,k) = \frac{1}{\hbar}\frac{\partial E(i,k)}{\partial k_\alpha} \quad (29)$$

$$m^* = \frac{\sigma}{e^2\tau} \quad (30)$$

Experimentally, the determination of effective mass is not an easy task. This is mainly based on the measurement of the cyclotron frequency (Equation 31). The sample is placed in a static

magnetic field, B. From a classical point of view, free charge carriers start to have a helicoidal motion with an angular frequency equal to the cyclotron frequency noted ω_c. From a quantum point of view, their energy levels are quantified and separated by a constant energy $\hbar\omega_c$.[220] Transitions between these states are possible under radio-frequency radiations, leading to the measurement of the cyclotron frequency and the determination of the effective mass.[220–225]

$$\omega_c = \frac{eB}{m^*} \tag{31}$$

To have a measurable cyclotron resonance, the mean free path of charge carriers must be large. Considering a charge carrier scattering time τ, it is assumed that the product $\omega_c\tau$ must be larger than 1 to lead to well-defined cyclotron resonance. In other words, the crystal must be as pure as possible and cool down below 100 K. Thus, this type of experiment is rather difficult for semiconductors synthesized as a powder with a large number of impurities; making the experimental determination of effective mass difficult to find for weakly investigated semiconductors.

Another approach has been proposed in 1966 by Zhitinskaya et al. to determine the effective mass of the charge carriers at the Fermi level from the experimental measurement of the Hall (R_H), Seebeck (α), conductivity (σ) and Nernst (Q) coefficients using the following formula (where q, $\hbar$, k_B and T are the charge of the particle, the reduced Planck constant, the Boltzmann constant and the temperature respectively):[226,227]

$$m^* = \left(\frac{3}{|R_H| q\pi}\right)^{\frac{2}{3}} \frac{q\hbar^2}{k_B^2 T}\left(\alpha - \frac{Q}{|R_H|\sigma}\right) \tag{32}$$

The demonstration of the equation presented above is based on the Boltzmann transport theory, thus the effective mass obtained in that way is a density averaged effective mass. This method to estimate the effective mass is sometimes called “the method of four coefficients” because it involves the knowledge of the four coefficients presented above. Because the

measurement of the Hall, Seebeck and conductivity coefficients is a kind of routine work in the field of thin solid films, the determination of effective mass using the equation (32) has been mainly employed by scientists in that field.[228–230] This experimental way to determine the effective mass can be applied to materials being less pure than the one used by the cyclotron resonance experiment, but the result is an averaged effective mass while the cyclotron resonance gives access to hole and electron effectives mass in several crystallographic directions.

Polaron. In terms of computational chemistry, the investigation of polaron conductivity is not easy in periodic systems. A charged system must be created to address the problem of treating such systems in periodic boundary conditions.[231–233] Then the charge must be localized, that is usually done first by distorting the geometry around the central atom and by adding a +U parameter on this atom. Next, the energy of the system is computed along several directions for the charge transfer (i.e., the hopping) to find the highest energy and define the activation energy. Because of all these steps, the simulation of hopping is difficult. Furthermore, this type of simulation is methodology dependent because of the charge compensation, because of the +U parameter and the initial distortion artificially imposed to localize the charge. Nevertheless, some examples are proposed in the literature for Ta_3N_5[200] (Figure 15), TiO_2[234], Fe_2O_3[235] or $BiVO_4$[236]. The main information extracted from this type of simulation is the influence of the crystallographic direction on the polaron diffusion and the activation energy for the thermal activation of the diffusion (Equation 25).

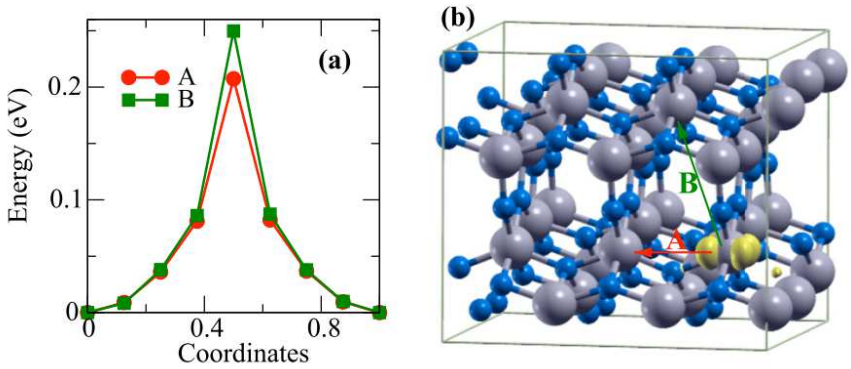

Figure 15. Simulation of the potential energy surface for the electron polaron hopping in two different directions (green and red curves) in Ta_3N_5. Figure reprinted with permission from [J. M. Morbec and G. Galli *Phys. Rev. B* 2016, 93, 035201]. Copyright (2018) The American Physical Society.

Some works solve some of the drawbacks of using periodic boundary conditions by extracting a cluster from the crystal structure and performing post-Hartree-Fock calculations (such as CASSCF).[237] The advantages of this approach are to avoid the problem of the electric charge in periodic boundary conditions and to use a more accurate method than DFT to investigate correlated materials. The drawback of the cluster approach is the removal of the Madelung potential of the infinite crystal that is known to have an important effect on charge-transfer states.

The activation energy of polaron hopping can be obtained experimentally by performing an Arrhenius analysis of charge carrier mobilities or conductivity.[238–241] The main difficulty is to attribute the activation energy to a specific mechanism since several mechanisms can be active for the conduction.

IV. Exciton binding energy.

The exciton is a quasi-particle developed in solid-state physics to describe the bound state between an electron and a hole. The formation of the exciton upon light absorption leads to a decrease of the fundamental gap energy, by an amount called exciton binding energy,

E_b,[242] explaining why the fundamental bandgap is larger than the optical one (Figure 4, equation 6). Excitons are generally classified in two categories depending on their delocalization: (i) The Mott-Wannier exciton delocalized on several unit cells and having a radius as high as several hundred of Å and generally having a relative low exciton binding energy (few meV). This is the exciton found in silicon. (ii) The Frenkel exciton, more localized (a radius of few Å) and generally having a large exciton binding energy (up to several eV). Other types of excitons can sometimes be defined in specific materials. The exciton plays an important role in photoelectrocatalysis since it must be dissociated to obtain free charge carriers that will be able to transport toward the surface of the semiconductor. To be dissociated efficiently at room temperature, the exciton must have a binding energy of the order of magnitude of the room thermal energy (k_BT ~ 25 meV) or lower. If E_b is notably larger, like in polymer semiconductors, the exciton cannot dissociate in the bulk material and must diffuse toward an interface to dissociate at this interface. This type of architecture is called bulk-heterojunction has been developed by the organic photovoltaic community.[243]

The most classical way to determine the exciton binding energy is by absorption or photoluminescence spectroscopy.[244] If the exciton is a Mott-Wannier one (i.e., delocalized on several unit-cells), researchers frequently compare it to a hydrogen atom, namely a positive (the hole) and a negative (the electron) charges interacting through the Coulomb potential, because the Hamiltonian of this exciton is the same as the one of the hydrogen atom. The hydrogen-like exciton has the same wavefunctions and energies as the hydrogen atom, adapted to the dielectric constant of the material and the hole mass (lighter than a proton). Due to the hydrogen-like nature of the exciton, it is sometimes possible to observe, in the absorption spectra of the semiconductor, energetic levels inside the fundamental bandgap associated with the hydrogen-like levels of the exciton. As a matter of illustration, we can

show the remarkable exciton spectroscopy measured in the Cu_2O crystal by Kazimierczuk et al. (Figure 16) confirming the hydrogen-like nature of excitons.[245]

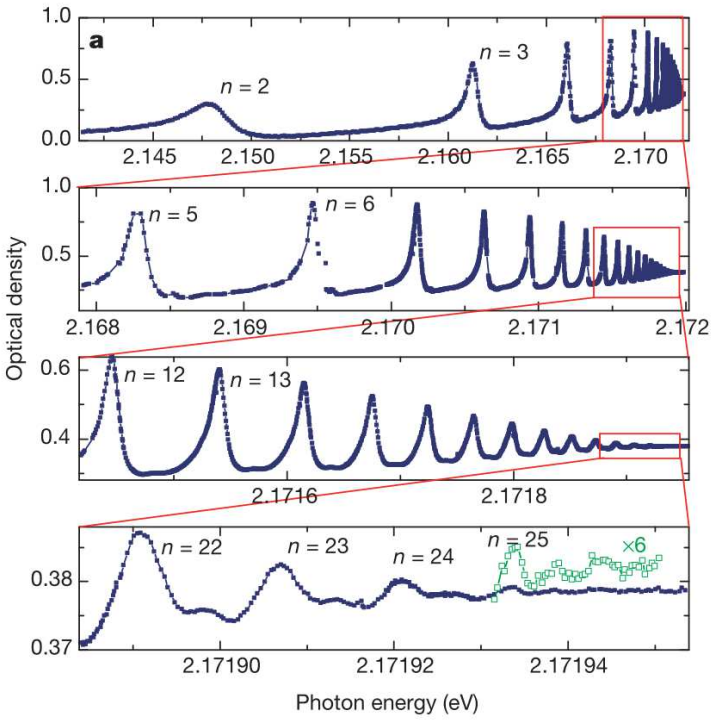

Figure 16. The high-resolution absorption spectrum of an exciton in Cu_2O measured at 1.2 K. The peak labeling "n" corresponds to the quantum number of the hydrogen-like levels of the exciton. Figure adapted with permission from [Kazimierczuk et al. *Nature* 2014, 514, 343]. Copyright (2018) Springer.

Some other less usual approaches can be used to determine exciton binding energies, such as STM spectroscopy[246] or UV-Vis spectroscopy under strong magnetic field (up to 65 T)[221,222]. In general, it is rather difficult to experimentally access exciton binding energies because of the good purity of the sample required and the very accurate spectroscopic measurements needed.

Due to the excited state nature of excitons, standard DFT, developed for ground state systems, is unable to treat them. Consequently, only theories developed to investigate excited states can perform a reliable analysis of exciton properties. These theories have been briefly presented in the discussion on bandgap simulations and are GW/BSE and TD-DFT methods. The BSE procedure (from Bethe-Salpeter Equations) is a post-treatment of the GW quasi-

768 particle calculation to get access to the exciton binding energy. The computation time of the
769 BSE procedure is similar to the TD-DFT one.[247] The efficiency of TD-DFT and GW/BSE
770 are not frequently compared in solid-state physics since TD-DFT is marginally used in that
771 field. Their comparison is more documented for molecular systems.[247–250] The recent
772 review of Blase *et al.* shows that hybrid functional generally gives optical gaps close to the
773 ones of GW/BSE.[117] In term of computational time, these approaches are now quite
774 similar, and because the large improvement performed in the recent years in the speed of
775 GW/BSE calculations, we can expect that in the near future, such calculations will be
776 performed in a daily manner.

777 If the exciton belongs to the Mott-Wannier category (i.e., delocalized on several unit
778 cells), it can be treated as a hydrogen atom (the hole being the proton) offering an analytical
779 formula for the binding energy.[37] In that model, the absolute value of the 1S state energy of
780 the exciton is its binding energy, E_b, and it can be computed with the formula:

781 $$E_b = -E_H \frac{\mu}{\varepsilon_r^2} \quad (33)$$

782 E_H is the energy of the 1s orbital of hydrogen (−13.6 eV), and μ is the reduced mass of the
783 exciton.

784 $$\frac{1}{\mu} = \frac{1}{m_e^*} + \frac{1}{m_h^*} \quad (34)$$

785 Consequently, if the dielectric constant and the effective masses of the semiconductor were
786 already computed, the exciton binding energy can be easily estimated through Formula 33.
787 The strength of this simple model is to highlight the dominant effect of the dielectric constant,
788 representing the ability of the material to screen charges, confirmed by more sophisticated
789 calculations.[251] The Mott-Wannier model has been used to compute the exciton binding
790 energy used to build Figure 5. As expected, hybrid functionals (global or range-separated)
791 lead the best agreement with the experiment, but with a standard deviation of around 30%.

This error is relatively large, but considering the simplicity of Formula (33), it is an excellent ratio precision/time. Of course, this model fails to predict Frenkel exciton binding energy. GW/BSE simulation of exciton binding energies has been compared to Mott-Wannier ones for C_3N_4 based-semiconductors (Figure 17).[252] The very large exciton binding energies were in agreement with the known Frenkel exciton character of this semiconductor. The error between the scGW/BSE exciton binding energy and the Mott-Wannier energy can reach 100%. But interestingly, while quantitatively wrong, the Mott-Wannier model succeed to predict the very large values of the exciton binding energy of this system, confirming that this approach could be used at least qualitatively.

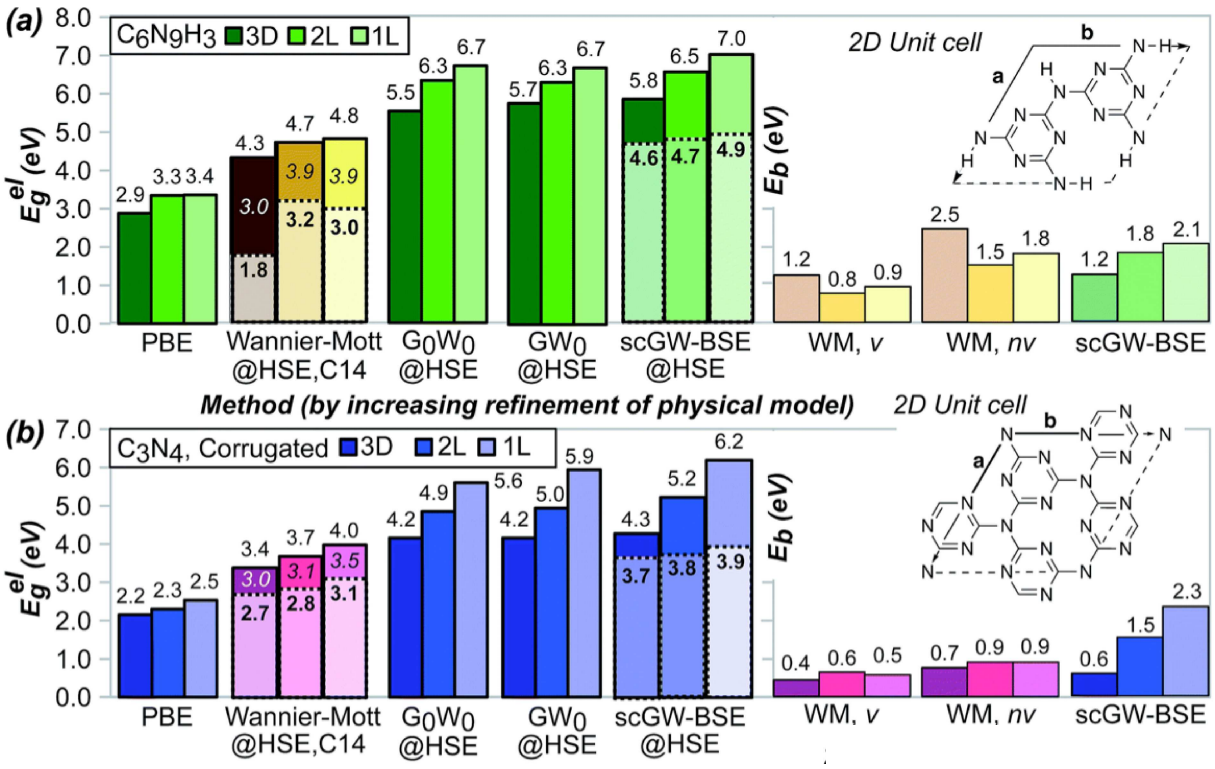

Figure 17. Electronic band gaps for (a) gt-$C_6N_9H_3$, (b) corrugated gt-C_3N_4 are reported. The Wannier-Mott analysis using the CRYSTAL14 code is depicted in an alternative color scheme. The optical band gaps $E_{opt,nv}$ g are depicted semi-transparently. The E_{vb}-corrected band gaps are provided in italics. The WM and scGW-BSE exciton binding energies E_b are provided to the right of the bandgaps, with v and nv denoting vibrationally and not vibrationally corrected, respectively. The 2D unit cells for the studied structures are given with lattice vectors a and b. Figure reprinted with permission from [S. T. A. G. Melissen et al. J. Mater. Chem. A 2017, 5, 5115-5122.] and The Royal Society of Chemistry.[95]

V. Band positions.

The ability of the semiconductor to perform the two half reactions of water splitting is related to the positions of the quasi-Fermi levels of the holes and electrons ($E_{F,h}$ and $E_{F,e}$ respectively) representing the chemical potentials of these two charge carriers. The quasi-Fermi levels are linked to the maximum of valence band (VBM) energy and minimum of conduction band (CBM) energy through the following equations where k_B is the Boltzmann constant, T the temperature, $N_{eff,c/v}$ the effective density of states of the conduction/valence band and $n_{e/h}$ the electron/hole concentration.

$$E_{F,e} = E_C - k_B T \ln\left(\frac{N_{eff,C}}{n_e}\right) \quad (35)$$

$$E_{F,h} = E_V + k_B T \ln\left(\frac{N_{eff,V}}{n_h}\right) \quad (36)$$

Osterloh proposes a thermodynamic interpretation of the previous formula where E_C and E_V are an enthalpy contribution to the chemical potentials and the logarithm term represents the entropic contribution.[53] The entropic contribution can be assimilated to the different ways to distribute particles in the effective states of the CBM and VBM. Those who are interested in the relationship between the different quantities (quasi-Fermi energies, chemical potentials, band positions, etc.) and the origin of this entropy contribution are invited to read the very clear publication of F. Osterloh.[53]

In general, N_{eff} is in the order of 10^{19} cm^{-3}.[228] The typical charge carrier density ranges from 10^{17}-10^{20} cm^{-3}.[253] As a consequence, the quasi-Fermi levels are very close to the position of the CBM and VBM and generally researchers in the field of photoelectrocatalysis assimilate the CBM and VBM to the redox potentials of the semiconductor. A better estimation of the redox potential involves the knowledge of N_{eff} and $n_{e/h}$ during the working of

the device. This is possible computationally to calculate N_{eff} from the band structure obtained by DFT [159] and to obtain $n_{e/h}$ by simulating the electron and flux inside the semiconductor [253] or by using semiconductors semiclassical equations [254]. Experimentally, quasi-Fermi energies can be obtained by impedance spectroscopy as explained by Bisquert et al.[65]

It is important to mention that quasi-Fermi energies, thus redox potentials, can change from the bulk to the surface due to the change in charge carrier concentrations because of their consumption for the HER and OER and because of charge transfer with the electrolyte.[255] This change is quantifiable only under a good simulation of $n_{e/h}$ or experimentally by an accurate fitting of the impedance spectra. For water splitting reaction, the potentials must be adapted to perform the two half-reactions, the HER and OER (equations 1 and 2).[256,257] As we can see in Figure 18,[55] some semiconductors, like WO_3, have suitable bandgap (~2.8 eV)[258], but their band positions (the conduction band in the case of WO_3) are not adapted to water splitting; this is why these properties are necessary to fully characterize a semiconductor.

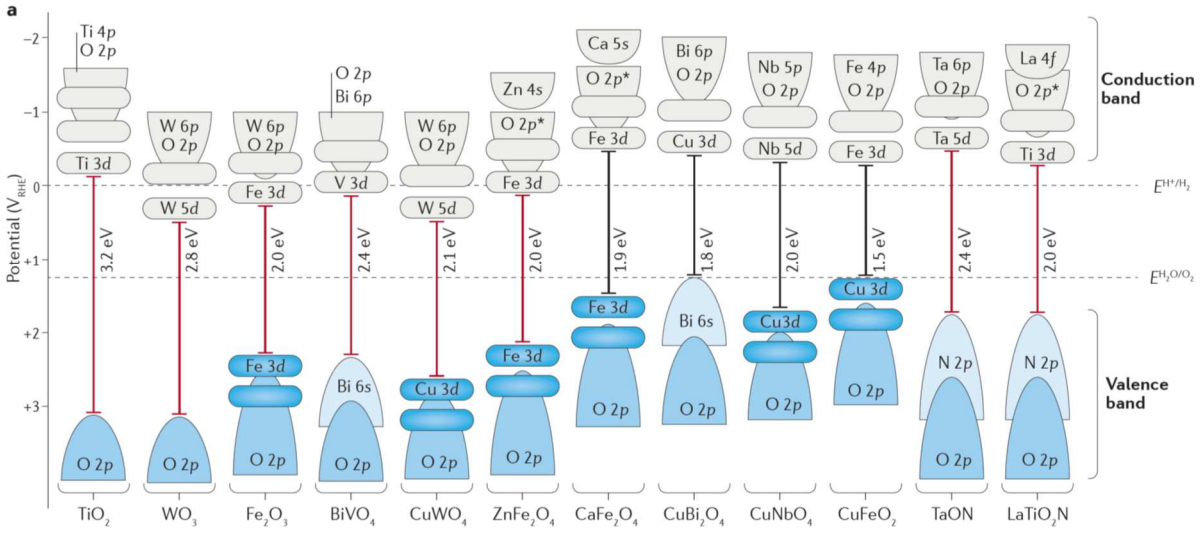

Figure 18. Band positions with respect to SHE reference of several semiconductors used for photoelectrocatalysis. Figure adapted with permission from [K. Sivula and R. vand de Krol, *Nat. Rev.* 2016, 1, 15010]. Copyright (2018) Springer.

The measurement of binding energies of occupied valence electrons is possible by conducting photoemission spectroscopies. This can then be translated to estimate the valence band maxima. One of the useful techniques is the photoelectron spectroscopy in the air (PESA)[259]; the measurement is easily conducted in the open air with relatively simple sample preparation. Accordingly, extra attention is necessary to check whether the surface is at an oxidized state, which might change the observed Fermi level. A similar method that requires ultrahigh vacuum (UHV) is ultraviolet photoelectron spectroscopy (UPS)[259,260]. The reference point can be the vacuum level, which is rationalized to obtain absolute potential, e.g., standard hydrogen electrode (SHE) potential is at –4.44 eV.[261]

In the form of photoelectrode, the flatband potential can be estimated from impedance spectroscopy using Mott-Schottky analysis.[262–266] The practical methodology can be found in the references.[164,267–269] In short, the space-charge capacity of the semiconductor, C, is given by the following equation;

$$\frac{1}{C^2} = \frac{1}{e\varepsilon_0\varepsilon_r A^2 N_D}\left(E_{app} - E_{FB} - \frac{kT}{e}\right) \tag{37}$$

where A is the surface area of the electrode, and E_{app} is the applied potential. By varying the applied potential, the Mott-Schottky plot, $1/C^2$ vs. the applied potential, is obtained and then the line is extrapolated when $1/C^2$ becomes zero to derive the flatband potential. The important aspect of the Mott-Schottky analysis is the fact that the measurement can be conducted with the sample immersed in liquid, and thus the conditions should reflect the actual situation of the relevant photoelectrocatalysis. The importance of the surface state, potentially determining ions and pH, was emphasized to significantly contribute to the determination of flatband potential.[270–274] Therefore, it is challenging to accurately interpret the Mott-Schottky analysis of the high surface area electrodes, typical for powder-semiconductor based electrodes. Similarly, there are some interesting discussions about the correlation of flatband potential with atomic electronegativities of oxide.[274]

In computational chemistry, one difficulty for defining the energy levels of semiconductors is to obtain the ionization potential and electron affinity with respect to a reference electrode. A first assumption frequently made is the Koopman's theorem assuming that the crystalline orbitals energy can be considered as the ionization potential and the electron affinity, as we have discussed in the bandgap section. The natural reference system used in quantum chemistry is the vacuum level, being at +4.44 V vs. SHE.[95,275,276] In a quantum chemical calculation, a part of the system must be a vacuum to have orbital energies obtained with respect to this reference. In other words, the band positions are not obtained for a bulk material but for a surface. Each computed band position depends on the surface chosen to be exposed to the vacuum, and the results are surface dependent, as illustrated by the work of Stevanovic et al.[277] (Figure 19). In general, quantum chemists choose non-polar surfaces because polar surfaces are prone to reconstruction and defects, and from a technical point of view, this leads to a non-stoichiometry or strong dipole moment, ultimately affecting the electronic structure, as can be seen in the case of $SrTiO_3$ in Figure 19.[277–285] As for the bandgap calculation, the only very accurate computational protocol can lead to reliable band positions, such as range-separated hybrid calculation or GW calculations.[148,159,277,278,286,287]

Even with the most accurate computational chemistry approach, to obtain a band position close to the experiment is not guaranteed. Indeed, the slab directly cut in the bulk material is frequently far to be a good model of the real surface. Surfaces can experience important reconstruction, especially for the polar ones, such as in the case of $SrTiO_3$, or change of composition compared to the bulk like for Ta_3N_5.[281,282,288] Furthermore, put into the electrolyte of water splitting device, the nature of the surface can change. Thus, determining the band edge positions can be a difficult task.

Figure 19. Calculated band edge energies (vs. vacuum) from GW single point calculations on top of PBE optimized surfaces. Experimental energies (obtained by photoemission) are given as bold lines. Figure reprinted with permission from [V. Stevanović et al. *Phys. Chem. Chem. Phys.* 2014, *16*, 3706–3714]. Copyright (2018) The Royal Society of Chemistry.

The description of a realistic interface by computational chemistry has been the subject of several developments, summarized by the review of Phan *et al.*[91] Modeling highlighted the influence of water adsorbed on the semiconductor surface on the electronic properties of the surface, including band positions.[289] The most important achievements in that field are clearly the description of the semiconductor/water interface by quantum chemical molecular dynamics.[290] This type of calculation has been applied to several types of semiconductors/electrolyte interfaces, such as the TiO_2/water interface simulation[291–293], Fe_2O_3/water interface simulation[294], ZnO/water interface simulation[295], and Al_2O_3/water interface simulation[296]. While *ab initio* molecular dynamics is probably the best tool to model the surface of the semiconductor placed in water, the very demanding computational resources and time prevent the use of this approach for high-throughput simulation of semiconductors. Another difficulty to manage during the simulation of the semiconductor/electrolyte interface is the electrolyte composition, frequently containing a large concentration of ions. Several approaches can be used to model such systems, including explicit simulation of the ions[297–299] or implicit simulation generally based on the Poisson-Boltzmann equations[300–304] of the electrolyte. The simulation of band positions will probably gain in reliability in the future due to the large work devoted to the simulation of surface/electrolyte interfaces.[255]

The band positions of semiconductors are also affected by the interaction of the surface with the co-catalyst deposited on the surface. This influence can be modeled by directly simulating the interface between the two materials, for example, the WO_3/IrO_2 interface by Ping et al.[305] and TiO_2/IrO_2 interface by Pastore et al.[306] In photocatalytic

water splitting, the decoration with active electrocatalysts is essential to achieve high efficiency, so this catalyst decoration must be taken into consideration. Since this local electronic structure generated at the catalyst-semiconductor interface is effectively utilized to separate charges, this should be a critical investigation for the future direction of the research in photoelectrocatalysis. Also, it is important to determine whether the interface is constructed with inclusion of an electrolyte (semiconductor-electrolyte interface) or effectively isolated with an electrolyte by a catalyst [91,307–309] or protecting layer.[310,311] Concurrent investigations on both experimental measurements and theoretical description of such complicated interface would be suggested to be the key for improved photocatalytic reactions.

Conclusions and perspectives.

New semiconductors are now frequently proposed in the literature for photocatalytic applications. A deep characterization of new semiconductors is important to assess their potentialities for the desired application. Unfortunately, these characterizations are sometimes lacking or performed using unreliable techniques. Collective efforts should be dedicated to establishing very reliable approaches to characterize semiconductors, both experimentally and theoretically. For some properties, the quantum chemical approaches have reached accuracy very close to the experiment with very reasonable computational resources. Those calculations should be performed for all newly synthesized semiconductors, such as to obtain a kind of identity card of the new material.

Computational chemistry can go beyond the characterization of a single material. Because the tools of quantum chemists have achieved a degree of precision close to the experiment, projects of high throughput prediction of materials properties are appearing.[312–317] The objective is to predict new materials with the desired properties before starting a long and costly experimental synthesis.

A complete semiconductor characterization is also necessary for multi-scale simulations. This type of modeling aims at simulating the full process of photoelectrocatalysis from light absorption to chemicals production[57,254,318–320] and involves several fields of physics and chemistry, as well as with several scales in space and time. Among the phenomena simulated by multi-scale modeling, charge carrier generation and transport in the semiconductor, leading to the flux of electrons and holes arriving at the surface of the semiconductor, are governed by semi-classical semiconductor equations involving several properties discussed in the manuscript (dielectric constants and mobilities).[253]

References

[1] G. Peng, M. Grätzel, M.K. Nazeeruddin, Organohalide Lead Perovskites for Photovoltaic Applications, Energy Environ. Sci. 7 (2014) 2448–2463. doi:10.1021/acs.jpclett.5b02893.

[2] A. Goetzberger, C. Hebling, H.-W. Schock, Photovoltaic materials, history, status and outlook, Mater. Sci. Eng. R. 40 (2003) 1–46. doi:10.1016/S0927-796X(02)00092-X.

[3] T. Ameri, N. Li, C.J. Brabec, Highly efficient organic tandem solar cells: a follow up review, Energy Environ. Sci. 6 (2013) 2390. doi:10.1039/c3ee40388b.

[4] M. Stuckelberger, R. Biron, N. Wyrsch, F.J. Haug, C. Ballif, Review: Progress in solar cells from hydrogenated amorphous silicon, Renew. Sustain. Energy Rev. 76 (2017) 1497–1523. doi:10.1016/j.rser.2016.11.190.

[5] A. Shah, P. Torres, R. Tscharner, N. Wyrsch, H. Keppner, Photovoltaic Technology : The Case for Thin-Film Solar Cells, Science 285 (1999) 692–699. doi:10.1126/science.285.5428.692.

[6] M.A. Green, Y. Hishikawa, E.D. Dunlop, D.H. Levi, J. Hohl-Ebinger, A.W.Y. Ho-Baillie, Solar cell efficiency tables (version 51), Prog. Photovolt Res. Appl. 26 (2018)

977 3–12. doi:10.1002/pip.2978.
978 [7] M. Grätzel, Recent advances in sensitized mesoscopic solar cells., Acc. Chem. Res. 42
979 (2009) 1788–1798. doi:10.1021/ar900141y.
980 [8] Photovotlaic Efficiency Chart, Natl. Renew. Energy Lab. (2018)
981 https://www.nrel.gov/pv/assets/images/efficiency-c.
982 [9] A. Nozik, Photoelectrochemistry: Applications to solar energy conversion, Annu. Rev.
983 Phys. Chem. 29 (1978) 189–222. doi:10.1146/annurev.pc.29.100178.001201.
984 [10] H. Yoneyama, Electrochemical aspects of light-induced heterogeneous reactions on
985 semiconductors, Crit. Rev. Solid State Mater. Sci. 18 (1993) 69–111.
986 doi:10.1080/10408439308243416.
987 [11] J. Schneider, M. Matsuoka, M. Takeuchi, J. Zhang, Y. Horiuchi, M. Anpo, D.W.
988 Bahnemann, Understanding TiO2 photocatalysis: Mechanisms and materials, Chem.
989 Rev. 114 (2014) 9919–9986. doi:10.1021/cr5001892.
990 [12] X. Lang, X. Chen, J. Zhao, Heterogeneous visible light photocatalysis for selective
991 organic transformations, Chem. Soc. Rev. 43 (2014) 473–486.
992 doi:10.1039/c3cs60188a.
993 [13] W. Tu, Y. Zhou, Z. Zou, Photocatalytic conversion of CO_2 into renewable hydrocarbon
994 fuels: State-of-the-art accomplishment, challenges, and prospects, Adv. Mater. 26
995 (2014) 4607–4626. doi:10.1002/adma.201400087.
996 [14] J. Yang, D. Wang, H. Han, C. Li, Roles of cocatalysts in photocatalysis and
997 photoelectrocatalysis, Acc. Chem. Res. 46 (2013) 1900–1909. doi:10.1021/ar300227e.
998 [15] C. Jiang, S.J.A. Moniz, A. Wang, T. Zhang, J. Tang, Photoelectrochemical devices for
999 solar water splitting-materials and challenges, Chem. Soc. Rev. 46 (2017) 4645–4660.
1000 doi:10.1039/c6cs00306k.
1001 [16] A. Kudo, Y. Miseki, Heterogeneous photocatalyst materials for water splitting, Chem.

1002 Soc. Rev. 38 (2009) 253–278. doi:10.1039/b800489g.
1003 [17] S.E. Braslavsky, Glossary of terms used in photochemistry, 3rd edition (IUPAC
1004 Recommendations 2006), Pure Appl. Chem. 79 (2007) 293–465.
1005 doi:10.1351/pac200779030293.
1006 [18] S.E. Braslavsky, A.M. Braun, A.E. Cassano, A. V. Emeline, M.I. Litter, L. Palmisano,
1007 V.N. Parmon, N. Serpone, Glossary of terms used in photocatalysis and radiation
1008 catalysis (IUPAC Recommendations 2011), Pure Appl. Chem. 83 (2011) 931–1014.
1009 doi:10.1351/PAC-REC-09-09-36.
1010 [19] H. Kisch, Semiconductor photocatalysis - Mechanistic and synthetic aspects, Angew.
1011 Chem. Int. Ed. 52 (2013) 812–847. doi:10.1002/anie.201201200.
1012 [20] S.N. Habisreutinger, L. Schmidt-Mende, J.K. Stolarczyk, Photocatalytic Reduction of
1013 CO_2 on TiO_2 and Other Semiconductors, Angew. Chem. Int. Ed. 52 (2013) 7372–7408.
1014 [21] A.J. Morris, G.J. Meyer, E. Fujita, Molecular approaches to the photocatalytic
1015 reduction of carbon dioxide for solar fuels., Acc. Chem. Res. 42 (2009) 1983–1994.
1016 doi:10.1021/ar9001679.
1017 [22] X. Chang, T. Wang, J. Gong, CO_2 photo-reduction: insights into CO_2 activation and
1018 reaction on surfaces of photocatalysts, Energy Environ. Sci. 9 (2016) 2177–2196.
1019 doi:10.1039/C6EE00383D.
1020 [23] X. Chen, S. Shen, L. Guo, S. Mao, Semiconductor-based photocatalytic hydrogen
1021 generation, Chem. Rev. 110 (2010) 6503–6570. doi:10.1021/cr1001645.
1022 [24] T. Hisatomi, J. Kubota, K. Domen, Recent advances in semiconductors for
1023 photocatalytic and photoelectrochemical water splitting, Chem. Soc. Rev. 43 (2014)
1024 7520–7535. doi:10.1039/C3CS60378D.
1025 [25] A.J. Bard, M.A. Fox, Artificial Photosynthesis: Solar Splitting of Water to Hydrogen
1026 and Oxygen Water Splitting, Acc. Chem. Res. 28 (1995) 141–145.

1027 doi:10.1021/ar00051a007.
1028 [26] S. Chen, T. Takata, K. Domen, Particulate photocatalysts for overall water splitting,
1029 Nat. Rev. Mater. 2 (2017) 1–17. doi:10.1038/natrevmats.2017.50.
1030 [27] Y. Tachibana, L. Vayssieres, J.R. Durrant, Artificial photosynthesis for solar water-
1031 splitting, Nat. Photonics. 6 (2012) 511–518. doi:10.1038/nphoton.2012.175.
1032 [28] J.C. Colmenares, R. Luque, Heterogeneous photocatalytic nanomaterials: Prospects
1033 and challenges in selective transformations of biomass-derived compounds, Chem.
1034 Soc. Rev. 43 (2014) 765–778. doi:10.1039/c3cs60262a.
1035 [29] N. Zhang, R. Ciriminna, M. Pagliaro, Y.J. Xu, Nanochemistry-derived Bi_2WO_6
1036 nanostructures: Towards production of sustainable chemicals and fuels induced by
1037 visible light, Chem. Soc. Rev. 43 (2014) 5276–5287. doi:10.1039/c4cs00056k.
1038 [30] S.H. Li, S. Liu, J.C. Colmenares, Y.J. Xu, A sustainable approach for lignin
1039 valorization by heterogeneous photocatalysis, Green Chem. 18 (2016) 594–607.
1040 doi:10.1039/c5gc02109j.
1041 [31] A. V. Puga, Photocatalytic production of hydrogen from biomass-derived feedstocks,
1042 Coord. Chem. Rev. 315 (2016) 1–66. doi:10.1016/j.ccr.2015.12.009.
1043 [32] F.E. Osterloh, Photocatalysis versus Photosynthesis: A Sensitivity Analysis of Devices
1044 for Solar Energy Conversion and Chemical Transformations, ACS Energy Lett. 2
1045 (2017) 445–453. doi:10.1021/acsenergylett.6b00665.
1046 [33] A.C. Nielander, M.R. Shaner, K.M. Papadantonakis, S.A. Francis, N.S. Lewis, A
1047 taxonomy for solar fuels generators, Energy Environ. Sci. 8 (2015) 16–25.
1048 doi:10.1039/c4ee02251c.
1049 [34] N.S. Lewis, Research opportunities to advance solar energy utilization, Science 351
1050 (2016) 353. doi:10.1126/science.aad1920.22.
1051 [35] H. Gerischer, The impact of semiconductors on the concepts of electrochemistry,

Electrochim. Acta. 35 (1990) 1677–1699. doi:10.1016/0013-4686(90)87067-C.

[36] C. Ding, J. Shi, Z. Wang, C. Li, Photoelectrocatalytic Water Splitting: Significance of Cocatalysts, Electrolyte, and Interfaces, ACS Catal. 7 (2017) 675–688. doi:10.1021/acscatal.6b03107.

[37] M.G. Walter, E.L. Warren, J.R. McKone, S.W. Boettcher, Q. Mi, E. a Santori, N.S. Lewis, Solar water splitting cells., Chem. Rev. 110 (2010) 6446–6473. doi:10.1021/cr1002326.

[38] H. Gerischer, A mechanism of electron hole pair separation in illuminated semiconductor particles, J. Phys. Chem. 88 (1984) 6096–6097. doi:10.1021/j150669a007.

[39] L. Brus, Electronic wave functions in semiconductor clusters: Experiment and theory, J. Phys. Chem. 90 (1986) 2555–2560. doi:10.1021/j100403a003.

[40] Y. Nosaka, Y. Ishizuka, H. Miyama, Separation Mechanism of a Photoinduced Electron-Hole Pair in Metal-Loaded Semiconductor Powders., Ber. Bunsen-Ges. Phys. Chem. 90 (1986) 1199–1204. doi:10.1002/bbpc.19860901216.

[41] R. Abe, Recent progress on photocatalytic and photoelectrochemical water splitting under visible light irradiation, J. Photochem. Photobiol. C. 11 (2010) 179–209. doi:10.1016/j.jphotochemrev.2011.02.003.

[42] F.E. Osterloh, Inorganic nanostructures for photoelectrochemical and photocatalytic water splitting, Chem. Soc. Rev. 42 (2013) 2294–2320. doi:10.1039/c2cs35266d.

[43] Y. Goto, T. Hisatomi, Q. Wang, T. Higashi, K. Ishikiriyama, T. Maeda, Y. Sakata, S. Okunaka, H. Tokudome, M. Katayama, S. Akiyama, H. Nishiyama, Y. Inoue, T. Takewaki, T. Setoyama, T. Minegishi, T. Takata, T. Yamada, K. Domen, A Particulate Photocatalyst Water-Splitting Panel for Large-Scale Solar Hydrogen Generation, Joule. 2 (2018) 509–520. doi:10.1016/j.joule.2017.12.009.

[44] B.A. Pinaud, J.D. Benck, L.C. Seitz, A.J. Forman, Z. Chen, T.G. Deutsch, B.D. James, K.N. Baum, G.N. Baum, S. Ardo, H. Wang, E. Miller, T.F. Jaramillo, Technical and economic feasibility of centralized facilities for solar hydrogen production via photocatalysis and photoelectrochemistry, Energy Environ. Sci. 6 (2013) 1983–2002. doi:10.1039/c3ee40831k.

[45] M.R. Shaner, H.A. Atwater, N.S. Lewis, E.W. McFarland, A comparative technoeconomic analysis of renewable hydrogen production using solar energy, Energy Environ. Sci. 9 (2016) 2354–2371. doi:10.1039/C5EE02573G.

[46] L.C. Seitz, Z. Chen, A.J. Forman, B.A. Pinaud, J.D. Benck, T.F. Jaramillo, Modeling practical performance limits of photoelectrochemical water splitting based on the current state of materials research, ChemSusChem. 7 (2014) 1372–1385. doi:10.1002/cssc.201301030.

[47] R. Sathre, C.D. Scown, W.R. Morrow, J.C. Stevens, I.D. Sharp, J.W. Ager, K. Walczak, F.A. Houle, J.B. Greenblatt, Life-cycle net energy assessment of large-scale hydrogen production via photoelectrochemical water splitting, Energy Environ. Sci. 7 (2014) 3264–3278. doi:10.1039/C4EE01019A.

[48] J.W. Ager, M.R. Shaner, K.A. Walczak, I.D. Sharp, S. Ardo, Experimental demonstrations of spontaneous, solar-driven photoelectrochemical water splitting, Energy Environ. Sci. 8 (2015) 2811–2824. doi:10.1039/c5ee00457h.

[49] K. Takanabe, Photocatalytic Water Splitting: Quantitative Approaches toward Photocatalyst by Design, ACS Catal. 7 (2017) 8006–8022. doi:10.1021/acscatal.7b02662.

[50] D.M. Fabian, S. Hu, N. Singh, F.A. Houle, T. Hisatomi, K. Domen, F.E. Osterloh, S. Ardo, Particle suspension reactors and materials for solar-driven water splitting, Energy Environ. Sci. 8 (2015) 2825–2850. doi:10.1039/C5EE01434D.

[51] K. Takanabe, Solar Water Splitting Using Semiconductor Photocatalyst Powders, Top. Curr. Chem. 35 (2017) 98–101. doi:10.1007/128.

[52] W.Y. Liang, Excitons, Phys. Educ. 5 (1970) 226.

[53] F.E. Osterloh, Maximum Theoretical Efficiency Limit of Photovoltaic Devices: Effect of Band Structure on Excited State Entropy, J. Phys. Chem. Lett. 5 (2014) 3354–3359. doi:10.1021/jz501740n.

[54] S.T. Omelchenko, Y. Tolstova, H.A. Atwater, N.S. Lewis, Excitonic effects in emerging photovoltaic materials: A case study in Cu_2O, ACS Energy Lett. 2 (2017) 431–437. doi:10.1021/acsenergylett.6b00704.

[55] K. Sivula, R. van de Krol, Semiconducting materials for photoelectrochemical energy conversion, Nat. Rev. Mater. 1 (2016) 15010. doi:10.1038/natrevmats.2015.10.

[56] S. Hu, C. Xiang, S. Haussener, A.D. Berger, N.S. Lewis, An analysis of the optimal band gaps of light absorbers in integrated tandem photoelectrochemical water-splitting systems, Energy Environ. Sci. 6 (2013) 2984–2993. doi:10.1039/c3ee40453f.

[57] S. Haussener, C. Xiang, J.M. Spurgeon, S. Ardo, N.S. Lewis, A.Z. Weber, Modeling, simulation, and design criteria for photoelectrochemical water-splitting systems, Energy Environ. Sci. 5 (2012) 9922–9935. doi:10.1039/c2ee23187e.

[58] W. Shockley, H.J. Queisser, Detailed Balance Limit of Efficiency of p-n Junction Solar Cells, J. Appl. Phys. 32 (1961) 510. doi:10.1063/1.1736034.

[59] P. Zhou, J. Yu, M. Jaroniec, All-solid-state Z-scheme photocatalytic systems, Adv. Mater. 26 (2014) 4920–4935. doi:10.1002/adma.201400288.

[60] H. Li, W. Tu, Y. Zhou, Z. Zou, Z-Scheme Photocatalytic Systems for Promoting Photocatalytic Performance: Recent Progress and Future Challenges, Adv. Sci. 3 (2016). doi:10.1002/advs.201500389.

[61] K. Maeda, Z-scheme water splitting using two different semiconductor photocatalysts,

ACS Catal. 3 (2013) 1486–1503. doi:10.1021/cs4002089.

[62] K. Maeda, M. Higashi, D. Lu, R. Abe, K. Domen, M. Higash, D. Lu, R. Abe, K. Domen, Efficient nonsacraficial water splitting through two-step photoexcitation by visible light using a modified oxynitride as a hydrogen evolution photocataylst, J. Am. Chem. Soc. 132 (2010) 5858–5868. doi:10.1021/ja1009025.

[63] T. Le Bahers, M. Rérat, P. Sautet, Semiconductors used in photovoltaic and photocatalytic devices: Assessing fundamental properties from DFT, J. Phys. Chem. C. 118 (2014) 5997–6008. doi:10.1021/jp409724c.

[64] O. Madelung, Semiconductors: Data Handbook, Third edit, Springer, 2004.

[65] J. Bisquert, Theory of the Impedance of Electron Diffusion and Recombination in a Thin Layer, J. Phys. Chem. B. 106 (2002) 325–333. doi:10.1021/jp011941g.

[66] R.H. Coridan, A.C. Nielander, S.A. Francis, M.T. McDowell, V. Dix, S.M. Chatman, N.S. Lewis, Methods for comparing the performance of energy-conversion systems for use in solar fuels and solar electricity generation, Energy Environ. Sci. 8 (2015) 2886–2901. doi:10.1039/c5ee00777a.

[67] M. Qureshi, A.T. Garcia-Esparza, T. Shinagawa, P. Sautet, T. Le Bahers, K. Takanabe, Contribution of electrolyte in nanoscale electrolysis of pure and buffered water by particulate photocatalysis, Sustain. Energy Fuels. 2 (2018) 2044–2052. doi:10.1039/C8SE00272J.

[68] T. Shinagawa, K. Takanabe, Towards versatile and sustainable hydrogen production via electrocatalytic water splitting: Electrolyte engineering, ChemSusChem. 10 (2017) 1318–1336. doi:10.1002/cssc.201601583.

[69] M. Hara, T. Kondo, M. Komoda, S. Ikeda, K. Shinohara, A. Tanaka, J.N. Kondo, K. Domen, M. Hara, K. Shinohara, A. Tanaka, Cu_2O as a photocatalyst for overall water splitting under visible light irradiation, Chem. Commun. 2 (1998) 357–358.

1152 doi:10.1039/a707440i.
1153 [70] F.E. Osterloh, Inorganic Materials as Catalysts for Photoelectrochemical Splitting of
1154 Water, Chem. Mater. 20 (2008) 35. doi:10.1021/cm7024203.
1155 [71] Q. Wang, T. Hisatomi, Q. Jia, H. Tokudome, M. Zhong, C. Wang, Z. Pan, T. Takata,
1156 M. Nakabayashi, N. Shibata, Y. Li, I.D. Sharp, A. Kudo, T. Yamada, K. Domen,
1157 Scalable water splitting on particulate photocatalyst sheets with a solar-to-hydrogen
1158 energy conversion efficiency exceeding 1%, Nat. Mater. 15 (2016) 611–615.
1159 doi:10.1038/nmat4589.
1160 [72] M. Li, Y. Yang, Y. Ling, W. Qiu, F. Wang, T. Liu, Y. Song, X. Liu, P. Fang, Y. Tong,
1161 Y. Li, K. Sivula, R. Zboril, F. Le Formal, R. Robert, A. Weidenkaff, J. Tucek, J.
1162 Frydrych, M. Grätzel, K. Sivula, R. Zboril, F. Le Formal, R. Robert, A. Weidenkaff, J.
1163 Tucek, J. Frydrych, M. Gra, Y. Ling, G. Wang, D.A. Wheeler, Z.J. Z., Y. Li,
1164 Photoelectrochemical Water Splitting with Mesoporous Hematite Prepared by a
1165 Solution-Based Colloidal Approach, Nano Lett. 132 (2010) 7436–7444.
1166 doi:10.1021/acs.nanolett.7b00184.
1167 [73] J. Brillet, J.H. Yum, M. Cornuz, T. Hisatomi, R. Solarska, J. Augustynski, M. Graetzel,
1168 K. Sivula, Highly efficient water splitting by a dual-absorber tandem cell, Nat.
1169 Photonics. 6 (2012) 824–828. doi:10.1038/nphoton.2012.265.
1170 [74] J.S. Hu, L.L. Ren, Y.G. Guo, H.P. Liang, A.M. Cao, L.J. Wan, C.L. Bai, Mass
1171 production and high photocatalytic activity of ZnS nanoporous nanoparticles, Angew.
1172 Chem. Int. Ed. 44 (2005) 1269–1273. doi:10.1002/anie.200462057.
1173 [75] N. Bao, L. Shen, T. Takata, K. Domen, Self-Templated Synthesis of Nanoporous CdS
1174 Nanostructures for Highly Efficient Photocatalytic Hydrogen Production under Visible
1175 Light Self-Templated Synthesis of Nanoporous CdS Nanostructures for Highly
1176 Efficient Photocatalytic Hydrogen Production under, Chem. Mater. (2008) 110–117.

doi:10.1021/cm7029344.

[76] T.A. Kandiel, D.H. Anjum, P. Sautet, T. Le Bahers, K. Takanabe, Electronic structure and photocatalytic activity of wurtzite Cu–Ga–S nanocrystals and their Zn substitution, J. Mater. Chem. A. 3 (2015) 8896–8904. doi:10.1039/C5TA01552A.

[77] S. Lardhi, A. Curutchet, L. Cavallo, M. Harb, T. Le Bahers, Ab initio assessment of Bi1-xRExCuOS (RE=La, Gd, Y, Lu) solid solutions as a semiconductor for photochemical water splitting, Phys. Chem. Chem. Phys. 19 (2017) 12321–12330. doi:10.1039/C7CP01684K.

[78] A. Baqais, A. Curutchet, A. Ziani, H. Ait Ahsaine, P. Sautet, K. Takanabe, T. Le Bahers, Bismuth Silver Oxysulfide for Photoconversion Applications: Structural and Optoelectronic Properties, Chem. Mater. 29 (2017). doi:10.1021/acs.chemmater.7b02664.

[79] S. Meng, X. Zhang, G. Zhang, Y. Wang, H. Zhang, F. Huang, Synthesis, Crystal Structure, and Photoelectric Properties of a New Layered Bismuth Oxysulfide, Inorg. Chem. 54 (2015) 5768–5773. doi:10.1021/acs.inorgchem.5b00436.

[80] A. Ishikawa, T. Takata, J.N. Kondo, M. Hara, H. Kobayashi, K. Domen, Oxysulfide Sm2Ti2S2O5 as a stable photocatalyst for water oxidation and reduction under visible light irradiation ($\lambda \leq 650$ nm), J. Am. Chem. Soc. 124 (2002) 13547–13553. doi:10.1021/ja0269643.

[81] E. Nurlaela, T. Shinagawa, M. Qureshi, D.S. Dhawale, K. Takanabe, Temperature Dependence of Electrocatalytic and Photocatalytic Oxygen Evolution Reaction Rates Using NiFe Oxide, ACS Catal. 6 (2016) 1713–1722. doi:10.1021/acscatal.5b02804.

[82] T. Hisatomi, J. Kubota, K. Domen, Recent advances in semiconductors for photocatalytic and photoelectrochemical water splitting, Chem. Soc. Rev. 43 (2014) 7520–7535. doi:10.1039/c3cs60378d.

[83] W.J. Ong, L.L. Tan, Y.H. Ng, S.T. Yong, S.P. Chai, Graphitic Carbon Nitride ($g-C_3N_4$)-Based Photocatalysts for Artificial Photosynthesis and Environmental Remediation: Are We a Step Closer to Achieving Sustainability?, Chem. Rev. 116 (2016) 7159–7329. doi:10.1021/acs.chemrev.6b00075.

[84] M.K. Bhunia, S. Melissen, M.R. Parida, P. Sarawade, J.-M. Basset, D.H. Anjum, O.F. Mohammed, P. Sautet, T. Le Bahers, K. Takanabe, Dendritic Tip-on Polytriazine-Based Carbon Nitride Photocatalyst with High Hydrogen Evolution Activity, Chem. Mater. 27 (2015) 8237. doi:10.1021/acs.chemmater.5b02974.

[85] K. Maeda, K. Teramura, T. Takata, M. Hara, N. Saito, K. Toda, Y. Inoue, H. Kobayashi, K. Domen, Overall Water Splitting on $(Ga_{1-x}Zn_x)(N_{1-x}O_x)$ Solid Solution Photocatalyst: Relationship between Physical Properties and Photocatalytic Activity, J. Phys. Chem. B. 109 (2005) 20504–20510. doi:10.1021/jp053499y.

[86] A. Fuertes, Metal oxynitrides as emerging materials with photocatalytic and electronic properties, Mater. Horiz. 2 (2015) 453–461. doi:10.1039/c5mh00046g.

[87] A. Ziani, C. Le Paven, L. Le Gendre, F. Marlec, R. Benzerga, F. Tessier, F. Cheviré, M.N. Hedhili, A.T. Garcia-Esparza, S. Melissen, P. Sautet, T. Le Bahers, K. Takanabe, Photophysical Properties of $SrTaO_2N$ Thin Films and Influence of Anion Ordering: A Joint Theoretical and Experimental Investigation, Chem. Mater. 29 (2017) 3989–3998. doi:10.1021/acs.chemmater.7b00414.

[88] X. Li, J. Yu, J. Low, Y. Fang, J. Xiao, X. Chen, Engineering heterogeneous semiconductors for solar water splitting, J. Mater. Chem. A. 3 (2015) 2485–2534. doi:10.1039/C4TA04461D.

[89] M.D. Bhatt, J.S. Lee, Recent theoretical progress in the development of photoanode materials for solar water splitting photoelectrochemical cells, J. Mater. Chem. A. 3 (2015) 10632–10659. doi:10.1039/c5ta00257e.

1227 [90] P. Liao, E.A. Carter, New concepts and modeling strategies to design and evaluate
1228 photo-electro-catalysts based on transition metal oxides, Chem. Soc. Rev. 42 (2013)
1229 2401–2422. doi:10.1039/c2cs35267b.
1230 [91] T.A. Pham, Y. Ping, G. Galli, Modelling heterogeneous interfaces for solar water
1231 splitting, Nat. Mater. 16 (2017) 401–408. doi:10.1038/NMAT4803.
1232 [92] P.D. Blood, R.D. Swenson, G.A. Voth, Factors influencing local membrane curvature
1233 induction by N-BAR domains as revealed by molecular dynamics simulations, Science
1234 (80-.). 95 (2008) 1866–1876. doi:10.1529/biophysj.107.121160.
1235 [93] A.T. Garcia-Esparza, N. Tyminska, R. Al Rahal Al Orabi, T. Le Bahers, Full in silico
1236 DFT characterization of lanthanum and yttrium based oxynitride semiconductors for
1237 solar fuels, J. Mater. Chem. C (2019). doi:10.1039/c8tc05749d.
1238 [94] A.J. Cohen, P. Mori-Sánchez, W. Yang, Challenges for density functional theory,
1239 Chem. Rev. 112 (2012) 289–320. doi:10.1021/cr200107z.
1240 [95] J.-L. Bredas, Mind the gap!, Mater. Horiz. 1 (2014) 17–19.
1241 doi:10.1039/C3MH00098B.
1242 [96] T. Koopmans, Uber die Zuordnung von Wellenfunktionen und Eigenwerten zu den
1243 Einzelnen Electronen eines Atoms, Physica. 1 (2013) 104–113. papers://dc5b7a66-
1244 c191-4125-90d3-2536c98d4438/Paper/p18270.
1245 [97] J.F. Janak, Proof that $\partial E / \partial n_i = \varepsilon_i$ in density-functional theory, Phys. Rev. B. 18
1246 (1978) 7165–7168. doi:10.1103/PhysRevB.18.7165.
1247 [98] J.P. Perdew, W. Yang, K. Burke, Z. Yang, E.K.U. Gross, M. Scheffler, G.E. Scuseria,
1248 T.M. Henderson, I.Y. Zhang, A. Ruzsinszky, H. Peng, J. Sun, E. Trushin, A. Görling,
1249 Understanding band gaps of solids in generalized Kohn–Sham theory, Proc. Natl.
1250 Acad. Sci. 114 (2017) 2801–2806. doi:10.1073/pnas.1621352114.
1251 [99] M. Shishkin, M. Marsman, G. Kresse, Accurate Quasiparticle Spectra from Self-

Consistent GW Calculations with Vertex Corrections, Phys. Rev. Lett. 99 (2007) 246403. doi:10.1103/PhysRevLett.99.246403.

[100] J. Paier, M. Marsman, K. Hummer, G. Kresse, I.C. Gerber, J.G. Angyán, Screened hybrid density functionals applied to solids, J. Chem. Phys. 124 (2006) 154709. doi:10.1063/1.2187006.

[101] F. Tran, P. Blaha, Accurate band gaps of semiconductors and insulators with a semilocal exchange-correlation potential, Phys. Rev. Lett. 102 (2009) 5–8. doi:10.1103/PhysRevLett.102.226401.

[102] X. Hai, J. Tahir-Kheli, W.A. Goddard, Accurate band gaps for semiconductors from density functional theory, J. Phys. Chem. Lett. 2 (2011) 212–217. doi:10.1021/jz101565j.

[103] A. Alkauskas, P. Broqvist, A. Pasquarello, Defect levels through hybrid density functionals: Insights and applications, Phys. Stat. Sol. 248 (2011) 775–789. doi:10.1002/pssb.201046195.

[104] M. Jain, J.R. Chelikowsky, S.G. Louie, Reliability of hybrid functionals in predicting band gaps, Phys. Rev. Lett. 107 (2011) 1–5. doi:10.1103/PhysRevLett.107.216806.

[105] F. Labat, I. Ciofini, C. Adamo, Modeling ZnO phases using a periodic approach: from bulk to surface and beyond., J. Chem. Phys. 131 (2009) 044708. doi:10.1063/1.3179752.

[106] F. Labat, P. Baranek, C. Domain, C. Minot, C. Adamo, Density functional theory analysis of the structural and electronic properties of TiO_2 rutile and anatase polytypes: performances of different exchange-correlation functionals., J. Chem. Phys. 126 (2007) 154703. doi:10.1063/1.2717168.

[107] F. Labat, P. Baranek, C. Adamo, Structural and electronic properties of selected rutile and anatase TiO_2 surfaces: An ab initio investigation, J. Chem. Theory Comput. 4

(2008) 341–352. doi:10.1021/ct700221w.

[108] R. Gaspari, F. Labat, L. Manna, C. Adamo, A. Cavalli, Semiconducting and optical properties of selected binary compounds by linear response DFT+U and hybrid functional methods, Theor. Chem. Acc. 135 (2016) 1–6. doi:10.1007/s00214-016-1833-9.

[109] J.P. Perdew, M. Ernzerhof, K. Burke, Rationale for mixing exact exchange with density functional approximations, J. Chem. Phys. 105 (1996) 9982–9984. doi:10.1063/1.472933.

[110] C. Adamo, V. Barone, Toward reliable density functional methods without adjustable parameters: The PBE0 model, J. Chem. Phys. 110 (1999) 6158–6170. doi:10.1063/1.478522.

[111] J. Heyd, G.E. Scuseria, M. Ernzerhof, Hybrid functionals based on a screened Coulomb potential, J. Chem. Phys. 118 (2003) 8207–8215. doi:10.1063/1.1564060.

[112] J. Heyd, G.E. Scuseria, M. Ernzerhof, Erratum: “Hybrid functionals based on a screened Coulomb potential” [J. Chem. Phys. 118, 8207 (2003)], J. Chem. Phys. 124 (2006) 219906. doi:10.1063/1.2204597.

[113] T. Yanai, D.P. Tew, N.C. Handy, A new hybrid exchange–correlation functional using the Coulomb-attenuating method (CAM-B3LYP), Chem. Phys. Lett. 393 (2008) 51–57. doi:10.1016/j.cplett.2004.06.011.

[114] R. Dovesi, B. Civalleri, R. Orlando, C. Roetti, V.R. Saunders, Ab Initio Quantum Simulation in Solid State Chemistry, ChemInform. 36 (2005). doi:10.1002/chin.200548226.

[115] F. Labat, I. Ciofini, H.P. Hratchian, M. Frisch, K. Raghavachari, C. Adamo, First principles modeling of eosin-loaded ZnO films: a step toward the understanding of dye-sensitized solar cell performances., J. Am. Chem. Soc. 131 (2009) 14290–14298.

doi:10.1021/ja902833s.

[116] R. Dovesi, A. Erba, R. Orlando, C.M. Zicovich-Wilson, B. Civalleri, L. Maschio, M. Rérat, S. Casassa, J. Baima, S. Salustro, B. Kirtman, Quantum-mechanical condensed matter simulations with CRYSTAL, WIREs Comput Mol Sci. 8 (2018) 1–36. doi:10.1002/wcms.1360.

[117] X. Blase, I. Duchemin, D. Jacquemin, The Bethe–Salpeter equation in chemistry: relations with TD-DFT, applications and challenges, Chem. Soc. Rev. (2018). doi:10.1039/C7CS00049A.

[118] J.C. Conesa, Band structures and nitrogen doping effects in zinc titanate photocatalysts, Catal. Today. 208 (2013) 11–18.

[119] M. Gerosa, C.E. Bottani, L. Caramella, G. Onida, C. Di Valentin, G. Pacchioni, Electronic structure and phase stability of oxide semiconductors: Performance of dielectric-dependent hybrid functional DFT, benchmarked against GW band structure calculations and experiments, Phys. Rev. B. 91 (2015) 1–15. doi:10.1103/PhysRevB.91.155201.

[120] E. Menéndez-Proupin, P. Palacios, P. Wahnón, J.C. Conesa, Self-consistent relativistic band structure of the $CH_3NH_3PbI_3$ perovskite, Phys. Rev. B. 90 (2014) 045207. doi:10.1103/PhysRevB.90.045207.

[121] J.H. Skone, M. Govoni, G. Galli, Self-consistent hybrid functional for condensed systems, Phys. Rev. B. 89 (2014) 1–12. doi:10.1103/PhysRevB.89.195112.

[122] D. Fritsch, B.J. Morgan, A. Walsh, Self-Consistent Hybrid Functional Calculations: Implications for Structural, Electronic, and Optical Properties of Oxide Semiconductors, Nanoscale Res. Lett. 12 (2017). doi:10.1186/s11671-016-1779-9.

[123] N.P. Brawand, M. Vörös, M. Govoni, G. Galli, Generalization of dielectric-Dependent hybrid functionals to finite systems, Phys. Rev. X. 6 (2016) 041002.

1327 doi:10.1103/PhysRevX.6.041002.
1328 [124] J.H. Skone, M. Govoni, G. Galli, Nonempirical range-separated hybrid functionals for
1329 solids and molecules, Phys. Rev. B. 93 (2016) 1–12.
1330 doi:10.1103/PhysRevB.93.235106.
1331 [125] P. Verma, D.G. Truhlar, HLE17: An Improved Local Exchange-Correlation Functional
1332 for Computing Semiconductor Band Gaps and Molecular Excitation Energies, J. Phys.
1333 Chem. C. 121 (2017) 7144–7154. doi:10.1021/acs.jpcc.7b01066.
1334 [126] A.D. Becke, E.R. Johnson, A simple effective potential for exchange, J. Chem. Phys.
1335 124 (2006). doi:10.1063/1.2213970.
1336 [127] J. Gräfenstein, D. Izotov, D. Cremer, Avoiding singularity problems associated with
1337 meta-GGA (generalized gradient approximation) exchange and correlation functionals
1338 containing the kinetic energy density, J. Chem. Phys. 127 (2007) 214103.
1339 doi:10.1063/1.2800011.
1340 [128] Z. Yang, H. Peng, J. Sun, J.P. Perdew, More realistic band gaps from meta-generalized
1341 gradient approximations : Only in a generalized Kohn-Sham scheme, Phys. Rev. B. 93
1342 (2016) 205205. doi:10.1103/PhysRevB.93.205205.
1343 [129] The VASP Manual, (2017). https://cms.mpi.univie.ac.at/wiki/index.php/METAGGA
1344 (accessed January 10, 2019).
1345 [130] P. Liao, E.A. Carter, Testing variations of the GW approximation on strongly
1346 correlated transition metal oxides: Hematite (α-Fe_2O_3) as a benchmark, Phys. Chem.
1347 Chem. Phys. 13 (2011) 15189–15199. doi:10.1039/c1cp20829b.
1348 [131] A. Filippetti, N.A. Spaldin, Self-interaction-corrected pseudopotential scheme for
1349 magnetic and strongly-correlated systems, Phys. Rev. B. 67 (2003) 15.
1350 doi:10.1103/PhysRevB.67.125109.
1351 [132] Y. Nohara, S. Yamamoto, T. Fujiwara, Electronic structure of perovskite-type

transition metal oxides $LaMO_3$ (M=Ti-Cu) by U+GW approximation, Phys. Rev. B. 79 (2009) 195110. doi:10.1103/PhysRevB.79.195110.

[133] V. Singh, M. Kosa, K. Majhi, D.T. Major, Putting DFT to the test: A first-principles study of electronic, magnetic, and optical properties of Co_3O_4, J. Chem. Theor. Comput. 11 (2015) 64–72. doi:10.1021/ct500770m.

[134] C. Rödl, F. Sottile, L. Reining, Quasiparticle excitations in the photoemission spectrum of CuO from first principles: A GW study, Phys. Rev. B. 91 (2015) 1–13. doi:10.1103/PhysRevB.91.045102.

[135] H. Jiang, Revisiting the GW approach to d-and f -electron oxides, Phys. Rev. B. 97 (2018) 245132. doi:10.1103/PhysRevB.97.245132.

[136] S. Petit, S.T.A.G. Melissen, L. Duclaux, M.T. Sougrati, T. Le Bahers, P. Sautet, D. Dambournet, O.J. Borkiewicz, C. Laberty-Robert, O. Durupthy, How Should Iron and Titanium Be Combined in Oxides to Improve Photoelectrochemical Properties?, J. Phys. Chem. C. 120 (2016) 24121. doi:10.1021/acs.jpcc.6b05794.

[137] S.L. Dudarev, S.Y. Savrasov, C.J. Humphreys, a. P. Sutton, Electron-energy-loss spectra and the structural stability of nickel oxide: An LSDA+U study, Phys. Rev. B. 57 (1998) 1505–1509. doi:10.1103/PhysRevB.57.1505.

[138] R. Hafner, Ab-Initio Simulations of Materials Using VASP : Density-Functional Theory and Beyond, J. Comput. Chem. 28 (2008) 2044–2078. doi:10.1002/jcc.

[139] A.I. Liechtenstein, V.I. Anisimov, J. Zaanen, Density-functional theory and strong interactions: Orbital ordering in Mott-Hubbard insulators, Phys. Rev. B. 52 (1995) 5467–5471. doi:10.1103/PhysRevB.52.R5467.

[140] H.J. Kulik, M. Cococcioni, D.A. Scherlis, N. Marzari, Density functional theory in transition-metal chemistry: A self-consistent hubbard U approach, Phys. Rev. Lett. 97 (2006) 1–4. doi:10.1103/PhysRevLett.97.103001.

[141] M.E. Arroyo-De Dompablo, A. Morales-Garca, M. Taravillo, DFT+U calculations of crystal lattice, electronic structure, and phase stability under pressure of TiO2 polymorphs, J. Chem. Phys. 135 (2011) 054503. doi:10.1063/1.3617244.

[142] N. Hamdad, H. Rozale, A. Lakdja, A. Chahed, O. Benhelal, New theoretical investigation on the electronic structure and magnetic interaction for both cubic $SrFeO_3$ and $CaFeO_3$ oxides: Comparison between GGA and GGA + U approaches, Superlattices Microstruct. 63 (2013) 182–196. doi:10.1016/j.spmi.2013.08.002.

[143] H. Noura, GGA+U-DFT+U modeling structural, electronic and magnetic properties investigation on the ferromagnetic and anti-ferromagnetic $BaFeO_3$ characteristics: Insights from First-principle calculation, Superlattices Microstruct. 76 (2014) 425–435. doi:10.1016/j.spmi.2014.10.004.

[144] G. Onida, L. Reining, A. Rubio, Electronic excitations : density-functional versus many-body Green ' s-function approaches, Rev. Mod. Phys. 74 (2002) 601–659.

[145] P. Scherpelz, M. Govoni, I. Hamada, G. Galli, Implementation and Validation of Fully Relativistic GW Calculations: Spin-Orbit Coupling in Molecules, Nanocrystals, and Solids, J. Chem. Theory Comput. 12 (2016) 3523–3544. doi:10.1021/acs.jctc.6b00114.

[146] M. Govoni, G. Galli, Large Scale GW Calculations, J. Chem. Theory Comput. 11 (2015) 2680–2696. doi:10.1021/ct500958p.

[147] M.S. Hybertsen, S.G. Louie, First-principles theory of quasiparticles: Calculation of band gaps in semiconductors and insulators, Phys. Rev. Lett. 55 (1985) 1418–1421. doi:10.1103/PhysRevLett.55.1418.

[148] Y. Ping, D. Rocca, G. Galli, Electronic excitations in light absorbers for photoelectrochemical energy conversion: First principles calculations based on many body perturbation theory, Chem. Soc. Rev. 42 (2013) 2437–2469. doi:10.1039/c3cs00007a.

[149] F. Aryasetiawan, O. Gunnarsson, Reports on Progress in Physics Related content, Rep. Prog. Phys. 61 (1998) 237–312. doi:10.1088/0034-4885/77/5/056502.

[150] E. Mosconi, P. Umari, F. De Angelis, Electronic and optical properties of $MAPbX_3$ perovskites (X = I, Br, Cl): a unified DFT and GW theoretical analysis, Phys. Chem. Chem. Phys. 18 (2016) 27158–27164. doi:10.1039/C6CP03969C.

[151] P. Umari, E. Mosconi, F. De Angelis, Relativistic GW calculations on $CH_3NH_3PbI_3$ and $CH_3NH_3SnI_3$ Perovskites for Solar Cell Applications, Sci. Rep. 4 (2014) 1–7. doi:10.1038/srep04467.

[152] M. Gajdoš, K. Hummer, G. Kresse, J. Furthmüller, F. Bechstedt, Linear optical properties in the projector-augmented wave methodology, Phys. Rev. B. 73 (2006) 045112. doi:10.1103/PhysRevB.73.045112.

[153] Y. Zhong, P. Wang, H. Mei, Z. Jia, N. Cheng, Electronic structures and optical properties of $Cu_{1-x}Ag_xInTe_2$(x = 0, 0.25, 0.5, 0.75 and 1) chalcopyrite compounds, Mater. Sci. Semicond. Process. 84 (2018) 42–49. doi:10.1016/j.mssp.2018.04.038.

[154] A. Walsh, Y. Yan, M.N. Huda, M.M. Al-Jassim, S.-H.H. Wei, Band Edge Electronic Structure of $BiVO_4$: Elucidating the Role of the Bi s and V d Orbitals, Chem. Mater. 21 (2009) 547–551. doi:10.1021/cm802894z.

[155] A. Du, Y.H. Ng, N.J. Bell, Z. Zhu, R. Amal, S.C. Smith, Hybrid graphene/titania nanocomposite: Interface charge transfer, hole doping, and sensitization for visible light response, J. Phys. Chem. Lett. 2 (2011) 894–899. doi:10.1021/jz2002698.

[156] B. Saparov, F. Hong, J.P. Sun, H.S. Duan, W. Meng, S. Cameron, I.G. Hill, Y. Yan, D.B. Mitzi, Thin-Film Preparation and Characterization of $Cs_3Sb_2I_9$: A Lead-Free Layered Perovskite Semiconductor, Chem. Mater. 27 (2015) 5622–5632. doi:10.1021/acs.chemmater.5b01989.

[157] M. Landmann, E. Rauls, W.G. Schmidt, The electronic structure and optical response

of rutile, anatase and brookite TiO_2, J. Phys. Cond. Mat. 24 (2012). doi:10.1088/0953-8984/24/19/195503.

[158] P.D. Borges, L.M.R. Scolfaro, H.W.L. Alves, E.F. da Silva, DFT study of the electronic, vibrational, and optical properties of SnO_2, Theor. Chem. Acc. 126 (2010) 39–44. doi:10.1007/s00214-009-0672-3.

[159] T. Le Bahers, S. Haller, T. Le Mercier, P. Barboux, Assessing the Use of BiCuOS for Photovoltaic Application: From DFT to Macroscopic Simulation, J. Phys. Chem. C. 119 (2015) 17585–17595. doi:10.1021/acs.jpcc.5b05551.

[160] E. Nurlaela, M. Harb, S. Del Gobbo, M. Vashishta, K. Takanabe, Combined experimental and theoretical assessments of the lattice dynamics and optoelectronics of TaON and Ta_3N_5, J. Solid State Chem. 229 (2015) 219–227. doi:10.1016/j.jssc.2015.06.029.

[161] J. Paier, M. Marsman, G. Kresse, Dielectric properties and excitons for extended systems from hybrid functionals, Phys. Rev. B. 78 (2008) 121201. doi:10.1103/PhysRevB.78.121201.

[162] A.M. Ferrari, R. Orlando, M. Rérat, Ab Initio Calculation of the Ultraviolet-Visible (UV-vis) Absorption Spectrum, Electron-Loss Function, and Reflectivity of Solids, J. Chem. Theor. Comput. 11 (2015) 3245–3258. doi:10.1021/acs.jctc.5b00199.

[163] S. Refaely-Abramson, M. Jain, S. Sharifzadeh, J.B. Neaton, L. Kronik, Solid-state optical absorption from optimally tuned time-dependent range-separated hybrid density functional theory, Phys. Rev. B. 92 (2015) 1–6. doi:10.1103/PhysRevB.92.081204.

[164] Z. Chen, H. Dinh, E. Miller, Photoelectrochemical Water Splitting, Springer, Springer-Verlag New York, 2013.

[165] R. Swanepoel, Determination of the thickness and optical constants of amorphous silicon, J. Phys. E Sci. Instrum. 16 (1983) 1214. doi:10.1088/0022-3735/16/12/023.

[166] J.F. Muth, J.H. Lee, I.K. Shmagin, R.M. Kolbas, H.C. Casey, B.P. Keller, U.K. Mishra, S.P. DenBaars, Absorption coefficient, energy gap, exciton binding energy, and recombination lifetime of GaN obtained from transmission measurements, Appl. Phys. Lett. 71 (1997) 2572–2574. doi:10.1063/1.120191.

[167] S.H. Wemple, J.A. Seman, Optical Transmission Through Multilayered Structures, Appl. Opt. 12 (1973) 2947–2949.

[168] J.F. Lodenquai, Determination of absorption coefficients of thin films, Sol. Energy. 53 (1994) 209–210. doi:10.1016/0038-092X(94)90483-9.

[169] K. Nama Manjunatha, S. Paul, Investigation of optical properties of nickel oxide thin films deposited on different substrates, Appl. Surf. Sci. 352 (2015) 10–15. doi:10.1016/j.apsusc.2015.03.092.

[170] V. Džimbeg-Malčić, Ž. Barbarić-Mikočević, K. Itrić, Kubelka-Munk theory in describing optical properties of paper, Tech. Gaz. 18 (2011) 117–124.

[171] D.J. Dahm, Interpreting Diffuse Reflectance and Transmittance: A Theoretical Introduction to Absorption Spectroscopy of Scattering Materials, IM Publications LLP, 2007.

[172] A.B. Murphy, Band-gap determination from diffuse reflectance measurements of semiconductor films, and application to photoelectrochemical water-splitting, Sol. Energy Mater. Sol. Cells. 91 (2007) 1326–1337. doi:10.1016/j.solmat.2007.05.005.

[173] M. Qureshi, K. Takanabe, Insights on measuring and reporting heterogeneous photocatalysis: Efficiency definitions and setup examples, Chem. Mater. 29 (2017) 158–167. doi:10.1021/acs.chemmater.6b02907.

[174] D.L. Wood, J. Tauc, Weak Absorption Tails in Amorphous Semicondcutors, Phys. Rev. B. 5 (1972) 3144–3151.

[175] E.F. Schubert, Light-Emitting Diodes (Second Edition), Cambridge University Press,

2006.

[176] A.B. Murphy, Band-gap determination from diffuse reflectance measurements of semiconductor films, and application to photoelectrochemical water-splitting, Sol. Energy. Mater. Sol. Cells. 91 (2007) 1326–1337. doi:10.1016/j.solmat.2007.05.005.

[177] S. Munir, S.M. Shah, H. Hussain, R. Ali khan, Effect of carrier concentration on the optical band gap of TiO_2 nanoparticles, Mater. Des. 92 (2016) 64–72. doi:10.1016/j.matdes.2015.12.022.

[178] S. Sanguinetti, M. Guzzi, M. Gurioli, Characterization of Semiconductor Heterostructures and Nanostructures (2nd edition), Elsevier Science, 2008.

[179] I. Vurgaftman, J.R. Meyer, L.R. Ram-Mohan, Band parameters for III-V compound semiconductors and their alloys, J. Appl. Phys. 89 (2001) 5815–5875. doi:10.1063/1.1368156.

[180] K.F. Young, H.P.R. Frederikse, Compilation of the Static Dielectric Constant of Inorganic Solids, J. Phys. Chem. Ref. Data. 2 (1973) 313–410. doi:10.1063/1.3253121.

[181] A. Wypych, I. Bobowska, M. Tracz, A. Opasinska, S. Kadlubowski, A. Krzywania-Kaliszewska, J. Grobelny, P. Wojciechowski, Dielectric properties and characterisation of titanium dioxide obtained by different chemistry methods, J. Nanomater. 2014 (2014). doi:10.1155/2014/124814.

[182] Y. Il Kim, W. Si, P.M. Woodward, E. Sutter, S. Park, T. Vogt, Epitaxial thin-film deposition and dielectric properties of the perovskite oxynitride BaTaO2N, Chem. Mater. 19 (2007) 618–623. doi:10.1021/cm062480k.

[183] J.M. Morbec, I. Narkeviciute, T.F. Jaramillo, G. Galli, Optoelectronic properties of Ta_3N_5: A joint theoretical and experimental study, Phys. Rev. B. 90 (2014) 1–10. doi:10.1103/PhysRevB.90.155204.

[184] M. Ferrero, M. Rérat, R. Orlando, R. Dovesi, Coupled perturbed Hartree-Fock for

1502 periodic systems: the role of symmetry and related computational aspects., J. Chem.
1503 Phys. 128 (2008) 014110. doi:10.1063/1.2817596.
1504 [185] M. Ferrero, M. Rérat, R. Orlando, R. Dovesi, The Calculation of Static Polarizabilities
1505 of 1-3D Periodic Compounds . The Implementation in the CRYSTAL Code, J.
1506 Comput. Chem. 29 (2008) 1450–1459. doi:10.1002/jcc.
1507 [186] L. Maschio, B. Kirtman, R. Orlando, M. Rèrat, Ab initio analytical infrared intensities
1508 for periodic systems through a coupled perturbed Hartree-Fock/Kohn-Sham method, J.
1509 Chem. Phys. 137 (2012). doi:10.1063/1.4767438.
1510 [187] R.W. Nunes, X. Gonze, Berry-phase treatment of the homogeneous electric field
1511 perturbation in insulators, Phys. Rev. B. 63 (2001) 155107.
1512 doi:10.1103/PhysRevB.63.155107.
1513 [188] F. Kootstra, P.L. De Boeij, J.G. Snijders, Application of time-dependent density-
1514 functional theory to the dielectric function of various nonmetallic crystals, Phys. Rev.
1515 B. 62 (2000) 7071–7083. doi:10.1103/PhysRevB.62.7071.
1516 [189] I. Petousis, W. Chen, G. Hautier, T. Graf, T.D. Schladt, K.A. Persson, F.B. Prinz,
1517 Benchmarking density functional perturbation theory to enable high-throughput
1518 screening of materials for dielectric constant and refractive index, Phys. Rev. B. 93
1519 (2016) 1–8. doi:10.1103/PhysRevB.93.115151.
1520 [190] I. Petousis, D. Mrdjenovich, E. Ballouz, M. Liu, D. Winston, W. Chen, T. Graf, T.D.
1521 Schladt, K.A. Persson, F.B. Prinz, High-throughput screening of inorganic compounds
1522 for the discovery of novel dielectric and optical materials, Sci. Data. 4 (2017) 160134.
1523 doi:10.1038/sdata.2016.134.
1524 [191] L. Maschio, B. Kirtman, R. Orlando, M. Rérat, Ab initio analytical infrared intensities
1525 for periodic systems through a coupled perturbed Hartree-Fock/Kohn-Sham method, J.
1526 Chem. Phys. 137 (2012) 204113. doi:10.1063/1.4767438.

[192] L. Kavan, M. Grätzel, S.E. Gilbert, C. Klemenz, H.J. Scheel, Electrochemical and photoelectrochemical investigation of single-crystal anatase, J. Am. Chem. Soc. 118 (1996) 6716–6723. doi:10.1021/ja9541721.

[193] Q. Wang, S. Ito, M. Grätzel, F. Fabregat-Santiago, I. Mora-Seró, J. Bisquert, T. Bessho, H. Imai, Characteristics of high efficiency dye-sensitized solar cells., J. Phys. Chem. B. 110 (2006) 25210–21. doi:10.1021/jp064256o.

[194] L. Kavan, B. O'Regan, A. Kay, M. Grätzel, Preparation of TiO_2(anatase) films on electrodes by anodic oxidative hydrolysis of $TiCl_3$, J. Electroanal. Chem. 346 (1993) 291–307. doi:10.1016/0022-0728(93)85020-H.

[195] S. Federal, Highly Efficient Semicondcuting TiO_2 Photoelectrodes Prepared by Aerosol Pyrolysis., Electrochim. Acta. 40 (1995) 643–652.

[196] A. Shluger, A. Stoneham, Small polarons in real cyrstals: concepts and probelms, J. Phys. Condens. Matter. 5 (1993) 3049–3086.

[197] S. Difley, L.-P. Wang, S. Yeganeh, S.R. Yost, T. Van Voorhis, Electronic properties of disordered organic semiconductors via QM/MM simulations., Acc. Chem. Res. 43 (2010) 995–1004. doi:10.1021/ar900246s.

[198] P.F. Barbara, T.J. Meyer, M.A. Ratner, Contemporary issues in electron transfer research, J. Phys. Chem. 100 (1996) 13148–13168. doi:10.1021/jp9605663.

[199] O. Ostroverkhova, Organic Optoelectronic Materials: Mechanisms and Applications, Chem. Rev. 116 (2016) 13279–13412. doi:10.1021/acs.chemrev.6b00127.

[200] J.M. Morbec, G. Galli, Charge transport properties of bulk Ta_3N_5 from first principles, Phys. Rev. B. 93 (2016) 035201. doi:10.1103/PhysRevB.93.035201.

[201] Z. Shuai, L. Wang, Q. Li, Evaluation of charge mobility in organic materials: From localized to delocalized descriptions at a first-principles level, Adv. Mat. 23 (2011) 1145–1153. doi:10.1002/adma.201003503.

[202] J. Lee, J.W. Chung, D.H. Kim, B.L. Lee, J. Il Park, S. Lee, R. Häusermann, B. Batlogg, S.S. Lee, I. Choi, I.W. Kim, M.S. Kang, Thin Films of Highly Planar Semiconductor Polymers Exhibiting Band-like Transport at Room Temperature, J. Am. Chem. Soc. 137 (2015) 7990–7993. doi:10.1021/jacs.5b04253.

[203] C. Kittel, Introduction to Solid State Physics, Global Edition, Wiley, Wiley, 1998.

[204] G. Hautier, A. Miglio, D. Waroquiers, G.M. Rignanese, X. Gonze, How does chemistry influence electron effective mass in oxides? A high-throughput computational analysis, Chem. Mater. 26 (2014) 5447–5458. doi:10.1021/cm404079a.

[205] J. Laflamme Janssen, Y. Gillet, S. Poncé, A. Martin, M. Torrent, X. Gonze, Precise effective masses from density functional perturbation theory, Phys. Rev. B. 93 (2016) 1–22. doi:10.1103/PhysRevB.93.205147.

[206] J. Feng, B. Xiao, Crystal Structures, Optical Properties, and Effective Mass Tensors of $CH_3NH_3PbX_3$ (X = I and Br) Phases Predicted from HSE06, J. Phys. Chem. Lett. 5 (2014) 1278–1282.

[207] M. Harb, A. Ziani, K. Takanabe, Critical difference between optoelectronic properties of α- and β-$SnWO_4$ semiconductors: A DFT/HSE06 and experimental investigation, Phys. Stat. Sol. B. 5 (2016) 1–5. doi:10.1002/pssb.201552774.

[208] Y.-S. Kim, K. Hummer, G. Kresse, Accurate band structures and effective masses for InP, InAs, and InSb using hybrid functionals, Phys. Rev. B. 80 (2009) 035203. doi:10.1103/PhysRevB.80.035203.

[209] M. Harb, Predicting suitable optoelectronic properties of monoclinic VON semiconductor crystals for photovoltaics using accurate first-principles computations, Phys. Chem. Chem. Phys. 17 (2015) 25244–25249. doi:10.1039/C5CP03924J.

[210] J. Gamon, D. Giaume, G. Wallez, J.-B. Labégorre, O.I. Lebedev, R. Al Rahal Al Orabi, S. Haller, T. Le Mercier, E. Guilmeau, A. Maignan, P. Barboux, Substituting Copper

with Silver in the BiMOCh Layered Compounds (M = Cu or Ag; Ch = S, Se, or Te): Crystal, Electronic Structure, and Optoelectronic Properties, Chem. Mater. 30 (2017) 549–558. doi:10.1021/acs.chemmater.7b04962.

[211] H. He, R. Orlando, M.A. Blanco, R. Pandey, E. Amzallag, I. Baraille, M. Rérat, First-principles study of the structural, electronic, and optical properties of Ga_2O_3 in its monoclinic and hexagonal phases, Phys. Rev. B. 74 (2006) 1–8. doi:10.1103/PhysRevB.74.195123.

[212] Y.S. Kim, M. Marsman, G. Kresse, F. Tran, P. Blaha, Towards efficient band structure and effective mass calculations for III-V direct band-gap semiconductors, Phys. Rev. B. 82 (2010) 1–11. doi:10.1103/PhysRevB.82.205212.

[213] A. Svane, N.E. Christensen, I. Gorczyca, M. Van Schilfgaarde, A.N. Chantis, T. Kotani, Quasiparticle self-consistent GW theory of III-V nitride semiconductors: Bands, gap bowing, and effective masses, Phys. Rev. B. 82 (2010) 1–6. doi:10.1103/PhysRevB.82.115102.

[214] M.R. Filip, C. Verdi, F. Giustino, GW Band Structures and Carrier Effective Masses of $CH_3NH_3PbI_3$and Hypothetical Perovskites of the Type $APbI_3$: A = NH_4, PH_4, AsH_4, and SbH_4, J. Phys. Chem. C. 119 (2015) 25209–25219. doi:10.1021/acs.jpcc.5b07891.

[215] E. Canadell, M.-L. Doublet, C. Iung, Orbital Approach to the Electronic Structure of Solids, Oxford Uni, Oxford University Press, 2012.

[216] V.A. Ha, F. Ricci, G.M. Rignanese, G. Hautier, Structural design principles for low hole effective mass s-orbital-based p-Type oxides, J. Phys. Chem. C. 5 (2017) 5772–5779. doi:10.1039/c7tc00528h.

[217] G.K.H. Madsen, D.J. Singh, BoltzTraP. A code for calculating band-structure dependent quantities, Comput. Phys. Commun. 175 (2006) 67–71. doi:10.1016/j.cpc.2006.03.007.

[218] T.J. Scheidemantel, C. Ambrosch-Draxl, T. Thonhauser, J. V. Badding, J.O. Sofo, Transport coefficients from first-principles calculations, Phys. Rev. B. 68 (2003) 125210. doi:10.1103/PhysRevB.68.125210.

[219] G. Pizzi, D. Volja, B. Kozinsky, M. Fornari, N. Marzari, An updated version of BOLTZWANN: A code for the evaluation of thermoelectric and electronic transport properties with a maximally-localized Wannier functions basis, Comput. Phys. Commun. 185 (2014) 2311–2312. doi:10.1016/j.cpc.2014.05.004.

[220] G. Dresselhaus, A.F. Kip, C. Kittel, Cyclotron resonance of electrons and holes in silicon and germanium crystals, Phys. Rev. 98 (1955) 368–384. doi:10.1103/PhysRev.98.368.

[221] K. Galkowski, A. Mitioglu, A. Miyata, P. Plochocka, O. Portugall, G.E. Eperon, J.T.W. Wang, T. Stergiopoulos, S.D. Stranks, H.J. Snaith, R.J. Nicholas, Determination of the exciton binding energy and effective masses for methylammonium and formamidinium lead tri-halide perovskite semiconductors, Energy Environ. Sci. 9 (2016) 962–970. doi:10.1039/c5ee03435c.

[222] A. Miyata, A. Mitioglu, P. Plochocka, O. Portugall, J.T.W. Wang, S.D. Stranks, H.J. Snaith, R.J. Nicholas, Direct measurement of the exciton binding energy and effective masses for charge carriers in organic-inorganic tri-halide perovskites, Nat. Phys. 11 (2015) 582–587. doi:10.1038/nphys3357.

[223] J. Merino, R.H. McKenzie, Cyclotron effective masses in layered metals, Phys. Rev. B. 62 (2000) 2416–2423. doi:10.1103/PhysRevB.62.2416.

[224] E. Rzepniewski, R.S. Edwards, J. Singleton, A. Ardavan, Y. Maeno, Cyclotron resonance in the layered perovskite superconductor Sr_2RuO_4, J. Phys. Cond. Mat. 14 (2002) 3759–3774. doi:10.1088/0953-8984/14/14/309.

[225] C. Schwab, A. Goltzene, On the Cyclotron Resonance of Carriers in Cu_2O, Phys. Stat.

Sol. 483 (1979) 483–487.

[226] I.A. Chernik, V.I. Kaidanov, N. V. Kolomoets, M.I. Vinogradova, Investigation of the valence band of lead telluride using transport phenomena, Sov. Phys. Semicond. 2 (1968) 645.

[227] M.K. Zhitinskaya, V.I. Kaidanov, I.A. Chernik, Nonparabolicity of the conduction band of lead telluride, Sov. Phys. Solid State. 8 (1966) 1160.

[228] M.H. Lee, K.H. Chang, H.C. Lin, Effective density-of-states distribution of polycrystalline silicon thin-film transistors under hot-carrier degradation, J. Appl. Phys. 102 (2007) 0–6. doi:10.1063/1.2777804.

[229] D.L. Young, H. Moutinho, Y. Yan, T.J. Coutts, D.L. Young, H. Moutinho, Y. Yan, T.J. Coutts, Growth and characterization of radio frequency magnetron sputter-deposited zinc thin films Growth and characterization of radio frequency magnetron sputter-deposited zinc stannate , Zn_2SnO_4 , thin films, J. Appl. Phys. 310 (2016) 310–319. doi:10.1063/1.1483104.

[230] Y. Tang, Z.M. Gibbs, L.A. Agapito, G. Li, H. Kim, M.B. Nardelli, S. Curtarolo, G.J. Snyder, performance in $CoSb_3$ skutterudites, Nat. Mater. 14 (2015) 1223–1228. doi:10.1038/NMAT4430.

[231] P.A. Schultz, Charged Local Defects in Extended Systems, Phys. Rev. B. 84 (2000) 1942–1945. doi:10.1103/PhysRevLett.84.1942.

[232] M. Jarvis, I. White, R. Godby, Supercell technique for total-energy calculations of finite charged and polar systems, Phys. Rev. B. 56 (1997) 14972–14978. doi:10.1103/PhysRevB.56.14972.

[233] C.L. Bailey, L. Liborio, G. Mallia, S. Tomić, N.M. Harrison, Defect physics of $CuGaS_2$, Phys. Rev. B. 81 (2010) 1–8. doi:10.1103/PhysRevB.81.205214.

[234] N.A. Deskins, M. Dupuis, Electron transport via polaron hopping in bulk TiO_2: A

density functional theory characterization, Phys. Rev. B. 75 (2007) 1–10. doi:10.1103/PhysRevB.75.195212.

[235] N. Iordanova, M. Dupuis, K.M. Rosso, Charge transport in metal oxides: A theoretical study of hematite α-Fe_2O_3, J. Chem. Phys. 122 (2005). doi:10.1063/1.1869492.

[236] K.E. Kweon, G.S. Hwang, J. Kim, S. Kim, S. Kim, Electron small polarons and their transport in bismuth vanadate: A first principles study, Phys. Chem. Chem. Phys. 17 (2015) 256–260. doi:10.1039/c4cp03666b.

[237] P. Liao, M.C. Toroker, E.A. Carter, Electron transport in pure and doped hematite, Nano Lett. 11 (2011) 1775–1781. doi:10.1021/nl200356n.

[238] N. Lu, L. Li, D. Geng, M. Liu, A review for polaron dependent charge transport in organic semiconductor, Org. Electron. Physics, Mater. Appl. 61 (2018) 223–234. doi:10.1016/j.orgel.2018.05.053.

[239] N. Zhao, Y.Y. Noh, J.F. Chang, M. Heeney, I. McCulloch, H. Sirringhaus, Polaron localization at interfaces in high-mobility microcrystalline conjugated polymers, Adv. Mater. 21 (2009) 3759–3763. doi:10.1002/adma.200900326.

[240] R.N. Sampaio, B.N. Dimarco, G.J. Meyer, Activation Energies for Electron Transfer from TiO_2 to Oxidized Dyes: A Surface Coverage Dependence Correlated with Lateral Hole Hopping, ACS Energ. Lett. 2 (2017) 2402–2407. doi:10.1021/acsenergylett.7b00759.

[241] A.J.E. Rettie, H.C. Lee, L.G. Marshall, J.F. Lin, C. Capan, J. Lindemuth, J.S. McCloy, J. Zhou, A.J. Bard, C.B. Mullins, Combined charge carrier transport and photoelectrochemical characterization of $BiVO_4$ single crystals: Intrinsic behavior of a complex metal oxide, J. Am. Chem. Soc. 135 (2013) 11389–11396. doi:10.1021/ja405550k.

[242] G. Bastard, E.E. Mendez, L.L. Chang, L. Esaki, Exciton binding energy in quantum

wells, Phys. Rev. B. 26 (1982) 1974–1979. doi:10.1103/PhysRevB.26.1974.

[243] T.M. Clarke, J.R. Durrant, Charge Photogeneration in Organic Solar Cells, Chem. Rev. 110 (2010) 6736–6767.

[244] A. Chernikov, T.C. Berkelbach, H.M. Hill, A. Rigosi, Y. Li, O.B. Aslan, D.R. Reichman, M.S. Hybertsen, T.F. Heinz, Exciton binding energy and nonhydrogenic Rydberg series in monolayer WS_2, Phys. Rev. Lett. 113 (2014) 1–5. doi:10.1103/PhysRevLett.113.076802.

[245] T. Kazimierczuk, D. Fröhlich, S. Scheel, H. Stolz, M. Bayer, Giant Rydberg excitons in the copper oxide Cu_2O, Nature. 514 (2014) 343–347. doi:10.1038/nature13832.

[246] S.F. Alvarado, P.F. Seidler, D.G. Lidzey, D.D.C. Bradley, Direct determination of the exciton binding energy of conjugated polymers using a scanning tunneling microscope, Phys. Rev. Lett. 81 (1998) 1082–1085. doi:10.1103/PhysRevLett.81.1082.

[247] D. Jacquemin, I. Duchemin, X. Blase, Benchmarking the Bethe-Salpeter Formalism on a Standard Organic Molecular Set, J. Chem. Theor. Comput. 11 (2015) 3290–3304. doi:10.1021/acs.jctc.5b00304.

[248] J. Li, G. D'Avino, A. Pershin, D. Jacquemin, I. Duchemin, D. Beljonne, X. Blase, Correlated electron-hole mechanism for molecular doping in organic semiconductors, Phys. Rev. Mater. 1 (2017) 025602. doi:10.1103/PhysRevMaterials.1.025602.

[249] D. Escudero, I. Duchemin, X. Blase, D. Jacquemin, Modeling the Photochrome-TiO2 Interface with Bethe-Salpeter and Time-Dependent Density Functional Theory Methods, J. Phys. Chem. Lett. 8 (2017) 936–940. doi:10.1021/acs.jpclett.7b00015.

[250] D. Jacquemin, I. Duchemin, X. Blase, 0-0 energies using hybrid schemes: Benchmarks of TD-DFT, CIS(D), ADC(2), CC2, and BSE/GW formalisms for 80 real-life compounds, J. Chem. Theor. Comput. 11 (2015) 5340–5359. doi:10.1021/acs.jctc.5b00619.

[251] M. Dvorak, S.H. Wei, Z. Wu, Origin of the variation of exciton binding energy in semiconductors, Phys. Rev. Lett. 110 (2013) 1–5. doi:10.1103/PhysRevLett.110.016402.

[252] S.N. Steinmann, S. Melissen, T. Le Bahers, P. Sautet, Challenges in Calculating the Bandgap of Triazine-Based Carbon Nitride Structures, J. Mater. Chem. A. 5 (2017) 5115–5122.

[253] A.T. Garcia-Esparza, K. Takanabe, A simplified theoretical guideline for overall water splitting using photocatalyst particles, J. Mater. Chem. A. 4 (2016) 2894–2908. doi:10.1039/C5TA06983A.

[254] P. Cendula, S.D. Tilley, S. Gimenez, J. Bisquert, M. Schmid, M. Gratzel, J.O. Schumacher, Calculation of the Energy Band Diagram of a Photoelectrochemical Water Splitting Cell, J. Phys. Chem. C. 118 (2014). doi:10.1021/jp509719d.

[255] J. Bisquert, P. Cendula, L. Bertoluzzi, S. Gimenez, Energy diagram of semiconductor/electrolyte junctions, J. Phys. Chem. Lett. 5 (2014) 205–207. doi:10.1021/jz402703d.

[256] C.G. van de Walle, J. Neugebauer, Universal alignment of hydrogen levels in semiconductors , insulators and solutions, Nature. 423 (2003) 626–628.

[257] K. Maeda, K. Domen, New non-oxide photocatalysts designed for overall water splitting under visible light, J. Phys. Chem. C. 111 (2007) 7851–7861. doi:10.1021/jp070911w.

[258] F. Wang, C. Di Valentin, G. Pacchioni, Electronic and structural properties of WO3: A systematic hybrid DFT study, J. Phys. Chem. C. 115 (2011) 8345–8353. doi:10.1021/jp201057m.

[259] M. Uda, Open Counter for Low Energy Electron Detection, J. Appl. Phys. Jpn. 24 (1985) 284–288. doi:10.7567/JJAPS.24S4.284.

[260] W.J. Chun, A. Ishikawa, H. Fujisawa, T. Takata, J.N. Kondo, M. Hara, M. Kawai, Y. Matsumoto, K. Domen, Conduction and valence band positions of Ta_2O_5, TaON, and Ta_3N_5 by UPS and electrochemical methods, J. Phys. Chem. B. 107 (2003) 1798–1803. doi:10.1021/jp027593f.

[261] S. Trasatti, The Absolute Electrode Potential : an Explanatory Note, Pure Appl. Phys. 58 (1986) 955–966. doi:10.1351/pac198658070955.

[262] W. Schottky, Zur Halbleitertheorie der Sperrschicht- und Spitzengleichrichter, Z. Phys. 113 (1939) 367–414.

[263] W. Schottky, Halbleitertheorie der Sperrschicht, Naturwissenschaften. 26 (1938) 843–843.

[264] N.F. Mott, Note on the Contact Between a Metal and an Insulator or Semi-Conductor, Cambridge Philos. Soc. 34 (1938) 568–572.

[265] J.A. Turner, Energetics of the Semiconductor-Electrolyte Interface, J. Chem. Educ. 60 (1983) 327–329. doi:10.1021/ed060p327.

[266] W.J. Albery, G.J. O'Shea, A.L. Smith, Interpretation and use of Mott-Schottky plots at the semiconductor/ electrolyte interface, J. Chem. Soc., Faraday Trans. 92 (1996) 4083–4085. doi:10.1039/ft9969204083.

[267] R. van de Krol, M. Grätzel, Photoelectro-chemical Hydrogen Production, Springer New York Dordrecht Heidelberg London, 2012.

[268] Z. Zhang, J.T. Yates, Band Bending in Semiconductor Chemical and Physical Consequences at Surfaces and Interfaces, Chem. Rev. 112 (2012) 5520–5551. doi:10.1021/cr3000626.

[269] K. Gelderman, L. Lee, S.W. Donne, Flat-Band Potential of a Semiconductor: Using the Mott–Schottky Equation, J. Chem. Educ. 84 (2007) 685. doi:10.1021/ed084p685.

[270] F. Cardon, W.P. Gomes, On the determination of the flat-band potential of a

semiconductor in contact with a metal or an electrolyte from the Mott-Schottky plot, J. Phys. D Appl. Phys. 11 (1978).

[271] P. Singh, R. Singh, R. Gale, K. Rajeshwar, J. DuBow, Surface charge and specific ion adsorption effects in photoelectrochemical devices, J. Appl. Phys. 51 (1980) 6286–6291. doi:10.1063/1.327616.

[272] Y. Matsumoto, T. Yoshikawa, E. ichi Sato, Dependence of the band bending of the oxide semiconductors on pH, J. Electrochem. Soc. 136 (1989) 1389–1391. doi:10.1149/1.2096927.

[273] G. Rothenberger, D. Fitzmaurice, M. Grätzel, Spectroscopy of conduction band electrons in transparent metal oxide semiconductor films: Optical determination of the flatband potential of colloidal titanium dioxide films, J. Phys. Chem. 96 (1992) 5983–5986. doi:10.1021/j100193a062.

[274] L. Kavan, M. Gra, S.E. Gilbert, C. Klemenz, H.J. Scheel, Electrochemical and Photoelectrochemical Investigation of Single-Crystal Anatase, J. Am. Chem. Soc. 118 (1996) 6716–6723.

[275] D. Cahen, A. Kahn, Electron energetics at surfaces and interfaces: Concepts and experiments, Adv. Mater. 15 (2003) 271–277. doi:10.1002/adma.200390065.

[276] A. Kahn, Fermi level, work function and vacuum level, Mater. Horizons. 3 (2016) 7–10. doi:10.1039/c5mh00160a.

[277] V. Stevanović, S. Lany, D.S. Ginley, W. Tumas, A. Zunger, Assessing capability of semiconductors to split water using ionization potentials and electron affinities only., Phys. Chem. Chem. Phys. 16 (2014) 3706–3714. doi:10.1039/c3cp54589j.

[278] Y. Hinuma, A. Gr, G. Kresse, F. Oba, Band alignment of semiconductors from density-functional theory and many-body perturbation theory, Phys. Rev. B. 90 (2014) 155405. doi:10.1103/PhysRevB.90.155405.

[279] C. Noguera, Polar oxide surfaces Claudine, J Phys. Condens Matter. 12 (2000) R367–R410.

[280] J.M.P. Martirez, S. Kim, E.H. Morales, B.T. Diroll, M. Cargnello, T.R. Gordon, C.B. Murray, D.A. Bonnell, A.M. Rappe, Synergistic oxygen evolving activity of a TiO_2-rich reconstructed $SrTiO_3$(001) surface, J. Am. Chem. Soc. 137 (2015) 2939–2947. doi:10.1021/ja511332y.

[281] N. Erdman, O. Warschkow, M. Asta, K.R. Poeppelmeier, D.E. Ellis, L.D. Marks, Surface structures of $SrTiO_3$(001): A TiO_2-rich reconstruction with a c(4 x 2) unit cell, J. Am. Chem. Soc. 125 (2003) 10050–10056. doi:10.1021/ja034933h.

[282] E. Heifets, R.I. Eglitis, E.A. Kotomin, J. Maier, G. Borstel, Ab initio modeling of surface structure for $SrTiO_3$ perovskite crystals, Phys. Rev. B. 64 (2001) 235417. doi:10.1103/PhysRevB.64.235417.

[283] H. Li, L.K. Schirra, J. Shim, H. Cheun, B. Kippelen, O.L.A. Monti, J.L. Bredas, Zinc oxide as a model transparent conducting oxide: A theoretical and experimental study of the impact of hydroxylation, vacancies, interstitials, and extrinsic doping on the electronic properties of the Polar ZnO (0002) surface, Chem. Mater. 24 (2012) 3044–3055. doi:10.1021/cm301596x.

[284] J. V. Lauritsen, S. Porsgaard, M.K. Rasmussen, M.C.R. Jensen, R. Bechstein, K. Meinander, B.S. Clausen, S. Helveg, R. Wahl, G. Kresse, F. Besenbacher, Stabilization principles for polar surfaces of ZnO, ACS Nano. 5 (2011) 5987–5994. doi:10.1021/nn2017606.

[285] P.W. Tasker, The stability of ionic crystal surfaces, J. Phys. C Solid State Phys. 12 (1979) 4977–4984. doi:10.1088/0022-3719/12/22/036.

[286] M. Harb, P. Sautet, E. Nurlaela, P. Raybaud, L. Cavallo, K. Domen, J.-M. Basset, K. Takanabe, Tuning the properties of visible-light-responsive tantalum (oxy)nitride

photocatalysts by non-stoichiometric compositions: a first-principles viewpoint, Phys. Chem. Chem. Phys. 16 (2014) 20548–20560. doi:10.1039/C4CP03594A.

[287] M.C. Toroker, D.K. Kanan, N. Alidoust, L.Y. Isseroff, P. Liao, E.A. Carter, First principles scheme to evaluate band edge positions in potential transition metal oxide photocatalysts and photoelectrodes, Phys. Chem. Chem. Phys. 13 (2011) 16644–16654. doi:10.1039/c1cp22128k.

[288] E. Nurlaela, S. Ould-Chikh, M. Harb, S. Del Gobbo, M. Aouine, E. Puzenat, P. Sautet, K. Domen, J.M. Basset, K. Takanabe, Critical role of the semiconductor-electrolyte interface in photocatalytic performance for water-splitting reactions using Ta3N5 particles, Chem. Mater. 26 (2014) 4812–4825. doi:10.1021/cm502015q.

[289] Y. Ping, R. Sundararaman, W.A. Goddard, Solvation effects on the band edge positions of photocatalysts from first principles, Phys. Chem. Chem. Phys. 17 (2015) 30499–30509. doi:10.1039/c5cp05740j.

[290] R. Car, M. Parrinello, Unified Approach for Molecular Dynamics and Density-Functional Theory, Phys. Rev. Lett. 55 (1985) 2471–2474. doi:10.1103/PhysRevLett.55.2471.

[291] J. Cheng, M. Sprik, The electric double layer at a rutile TiO_2 water interface modelled using density functional theory based molecular dynamics simulation, J. Phys. Cond. Mat. 26 (2014). doi:10.1088/0953-8984/26/24/244108.

[292] J. Cheng, M. Sprik, Aligning electronic energy levels at the TiO_2/H_2O interface, Phys. Rev. B. 82 (2010) 1–4. doi:10.1103/PhysRevB.82.081406.

[293] C. Sun, L.-M. Liu, A. Selloni, G.Q. (Max) Lu, S.C. Smith, Titania-water interactions: a review of theoretical studies, J. Mater. Chem. 20 (2010) 10319. doi:10.1039/c0jm01491e.

[294] N.J. English, M. Rahman, N. Wadnerkar, J.M.D. Macelroy, Photo-active and

dynamical properties of hematite (Fe_2O_3)-water interfaces: An experimental and theoretical study, Phys. Chem. Chem. Phys. 16 (2014) 14445–14454. doi:10.1039/c3cp54700k.

[295] N. Kharche, J.T. Muckerman, M.S. Hybertsen, First-principles approach to calculating energy level alignment at aqueous semiconductor interfaces, Phys. Rev. Lett. 113 (2014) 1–6. doi:10.1103/PhysRevLett.113.176802.

[296] P. Huang, T.A. Pham, G. Galli, E. Schwegler, Alumina(0001)/Water Interface: Structural Properties and Infrared Spectra from First-Principles Molecular Dynamics Simulations, J. Phys. Chem. C. 118 (2014) 8944–8951. doi:10.1021/jp4123002.

[297] D. Opalka, T.A. Pham, M. Sprik, G. Galli, The ionization potential of aqueous hydroxide computed using many-body perturbation theory, J. Chem. Phys. 141 (2014) 3–7. doi:10.1063/1.4887259.

[298] Q. Wan, L. Spanu, F. Gygi, G. Galli, Electronic structure of aqueous sulfuric acid from first-principles simulations with hybrid functionals, J. Phys. Chem. Lett. 5 (2014) 2562–2567. doi:10.1021/jz501168p.

[299] A.P. Gaiduk, C. Zhang, F. Gygi, G. Galli, Structural and electronic properties of aqueous NaCl solutions from ab initio molecular dynamics simulations with hybrid density functionals, Chem. Phys. Lett. 604 (2014) 89–96. doi:10.1016/j.cplett.2014.04.037.

[300] I. Borukhov, D. Andelman, H. Orland, Steric effects in electrolytes: A modified poisson-boltzmann equation, Phys. Rev. Lett. 79 (1997) 435–438. doi:10.1103/PhysRevLett.79.435.

[301] R. Jinnouchi, A.B. Anderson, Electronic structure calculations of liquid-solid interfaces: Combination of density functional theory and modified Poisson-Boltzmann theory, Phys. Rev. B. 77 (2008). doi:10.1103/PhysRevB.77.245417.

[302] D. Gunceler, K. Letchworth-Weaver, R. Sundararaman, K.A. Schwarz, T.A. Arias, The importance of nonlinear fluid response in joint density-functional theory studies of battery systems, Model. Simul. Mater. Sci. Eng. 21 (2013). doi:10.1088/0965-0393/21/7/074005.

[303] R. Sundararaman, K. Schwarz, Evaluating continuum solvation models for the electrode-electrolyte interface: Challenges and strategies for improvement, J. Chem. Phys. 146 (2017). doi:10.1063/1.4976971.

[304] S. Ringe, H. Oberhofer, K. Reuter, Transferable ionic parameters for first-principles Poisson-Boltzmann solvation calculations: Neutral solutes in aqueous monovalent salt solutions, J. Chem. Phys. 146 (2017). doi:10.1063/1.4978850.

[305] Y. Ping, W.A. Goddard, G.A. Galli, Energetics and solvation effects at the photoanode/catalyst interface: Ohmic contact versus Schottky barrier, J. Am. Chem. Soc. 137 (2015) 5264–5267. doi:10.1021/jacs.5b00798.

[306] M. Pastore, F. De Angelis, First-principles modeling of a dye-sensitized TiO_2/IrO_2 photoanode for water oxidation, J. Am. Chem. Soc. 137 (2015) 5798–5809. doi:10.1021/jacs.5b02128.

[307] Y. Nakato, H. Tsubomura, Structures and functions of thin metal layers on semiconductor electrodes, J. Photochem. 29 (1985) 257–266. doi:10.1016/0047-2670(85)87076-3.

[308] T.J. Mills, F. Lin, S.W. Boettcher, Theory and simulations of electrocatalyst-coated semiconductor electrodes for solar water splitting, Phys. Rev. Lett. 112 (2014) 1–5. doi:10.1103/PhysRevLett.112.148304.

[309] S.M. Sze, N. Kwok, Physics Of Semiconductor Devices, 3rd Ed, BWSTM, 2008.

[310] S. Hu, M.R. Shaner, J.A. Beardslee, M. Lichterman, B.S. Brunschwig, N.S. Lewis, Amorphous TiO2 coatings stabilize Si, GaAs, and GaP photoanodes for efficient water

oxidation, Science. 344 (2014) 1005–1009. doi:10.1126/science.1251428.

[311] N.Y. Labrador, X. Li, Y. Liu, H. Tan, R. Wang, J.T. Koberstein, T.P. Moffat, D. V. Esposito, Enhanced Performance of Si MIS Photocathodes Containing Oxide-Coated Nanoparticle Electrocatalysts, Nano Lett. 16 (2016) 6452–6459. doi:10.1021/acs.nanolett.6b02909.

[312] A.K. Singh, K. Mathew, H.L. Zhuang, R.G. Hennig, Computational screening of 2D materials for photocatalysis, J. Phys. Chem. Lett. 6 (2015) 1087–1098. doi:10.1021/jz502646d.

[313] A. Jain, I.E. Castelli, G. Hautier, D.H. Bailey, K.W. Jacobsen, Performance of genetic algorithms in search for water splitting perovskites, J. Mater. Sci. 48 (2013) 6519–6534. doi:10.1007/s10853-013-7448-9.

[314] J. Greeley, T.F. Jaramillo, J. Bonde, I. Chorkendorff, J.K. Nørskov, Computational high-throughput screening of electrocatalytic materials for hydrogen evolution, Nat. Mater. 5 (2006) 909–913. doi:10.1038/nmat1752.

[315] A.A. Emery, J.E. Saal, S. Kirklin, V.I. Hegde, C. Wolverton, High-Throughput Computational Screening of Perovskites for Thermochemical Water Splitting Applications, Chem. Mater. 28 (2016) 5621–5634. doi:10.1021/acs.chemmater.6b01182.

[316] K. Choudhary, I. Kalish, R. Beams, F. Tavazza, High-throughput Identification and Characterization of Two-dimensional Materials using Density functional theory, Sci. Rep. 7 (2017) 1–16. doi:10.1038/s41598-017-05402-0.

[317] I.E. Castelli, D.D. Landis, K.S. Thygesen, S. Dahl, I. Chorkendorff, T.F. Jaramillo, K.W. Jacobsen, New cubic perovskites for one- and two-photon water splitting using the computational materials repository, Energy Environ. Sci. 5 (2012) 9034–9043. doi:10.1039/c2ee22341d.

[318] Y.K. Gaudy, S. Dilger, S. Landsmann, U. Aschauer, S. Pokrant, S. Haussener, Determination and optimization of material parameters of particle-based $LaTiO_2N$ photoelectrodes, J. Mater. Chem. A. (2018). doi:10.1039/C8TA03649G.

[319] S. Haussener, S. Hu, C. Xiang, A.Z. Weber, N.S. Lewis, Simulations of the irradiation and temperature dependence of the efficiency of tandem photoelectrochemical water-splitting systems, Energy Environ. Sci. 6 (2013) 3605–3618. doi:10.1039/c3ee41302k.

[320] Y.K. Gaudy, S. Haussener, Utilizing modeling, experiments, and statistics for the analysis of water-splitting photoelectrodes, J. Mater. Chem. A. 4 (2016) 3100–3114. doi:10.1039/c5ta07328f.